

Automated Side Channel Analysis of Media Software with Manifold Learning *

Yuanyuan Yuan, Qi Pang, Shuai Wang†
The Hong Kong University of Science and Technology
{yyuanaq, qpangaa, shuaiw}@cse.ust.hk

arXiv:2112.04947v2 [cs.CR] 10 Dec 2021

Abstract

The prosperous development of cloud computing and machine learning as a service has led to the widespread use of media software to process confidential media data. This paper explores an adversary's ability to launch side channel analyses (SCA) against media software to reconstruct confidential media inputs. Recent advances in representation learning and perceptual learning inspired us to consider the reconstruction of media inputs from side channel traces as a *cross-modality manifold learning* task that can be addressed in a unified manner with an autoencoder framework trained to learn the mapping between media inputs and side channel observations. We further enhance the autoencoder with *attention* to localize the program points that make the primary contribution to SCA, thus automatically pinpointing information-leakage points in media software. We also propose a novel and highly effective defensive technique called *perception blinding* that can perturb media inputs with perception masks and mitigate manifold learning-based SCA.

Our evaluation exploits three popular media software to reconstruct inputs in image, audio, and text formats. We analyze three common side channels — cache bank, cache line, and page tables — and userspace-only cache set accesses logged by standard `Prime+Probe`. Our framework successfully reconstructs high-quality confidential inputs from the assessed media software and automatically pinpoint their vulnerable program points, many of which are unknown to the public. We further show that perception blinding can mitigate manifold learning-based SCA with negligible extra cost.

1 Introduction

Side channel analysis (SCA) infers program secrets by analyzing the target software's influence on physical computational characteristics, such as the execution time, accessed cache units, and power consumption. Practical SCA attacks have been launched on real-world crypto systems [74, 116, 121] to recover crypto keys. With the adoption of cloud computing and machine learning as a service (MLaaS), media software, a type of application software used for processing media files like images and text, is commonly involved in processing private data uploaded to cloud (e.g., for medical diagnosis). Existing works have exploited media software with extensive manual efforts or reconstruct only certain media data [45, 117, 123]. However, the community lacks a systematic and thorough understanding of SCA attack vectors for media software and of the ways that private user inputs of various types (e.g., images or text) can be reconstructed in a unified and automated manner. Hence, this is the first study toward media software of various input formats to assess how their inputs, which represent private user data, can be leaked via SCA in a fully automatic way.

Recent advances in representation learning and perceptual learning [15, 125] inspired us to recast SCA of media software as a cross-modality manifold learning task in which an autoencoder [50] is used to learn the mapping between confidential media inputs and the derived side channel traces in an end-to-end manner. The autoencoder framework can learn a low-dimensional joint manifold of media data and side channel observations to capture a highly expressive representation that is generally immune to noise.

Our proposed autoencoder framework is highly flexible. It converts side channel traces into latent representations with an encoder module ϕ_θ, and the media data in image, audio and text formats can be reconstructed by assembling decoders ψ_θ that correspond to various media data formats to ϕ_θ. Furthermore, by enhancing encoder ϕ_θ with attention [114], the autoencoder framework can automatically localize program points that make primary contributions to the reconstruction of media inputs. That is, the attention mechanism delivers a "bug detector" to locate program points at which information can leak.

Further, the observation that manifold learning captures key perceptions of high-dimensional data in a low-dimensional space [125] inspired us to propose the use of *perception*

*The extended version of the USENIX Security 2022 paper [122].
†Corresponding author.

blinding to mitigate manifold learning–based SCA. Well-designed perception blinding "dominates" the projected low-dimensional perceptions and thus confines adversaries to only generate media data perceptually bounded to the mask. In contrast, media software that is typically used to process data bytes of media data experiences no extra difficulty in processing the blinded data and recovering the original outputs.

Our evaluation exploits media software, including `libjpeg` [69], `FFmpeg` [1], and `Hunspell` [2], widely used to process media data in image, audio, and text formats. We assess these media software with regard to a common threat model in which *trace-based* attackers [20, 36, 54, 105] can log a trace of CPU cache banks, cache lines, or OS page-table entries accessed during the execution of media software. Moreover, we also launch standard `Prime+Probe` attack [102] in userspace-only scenarios and use the logged cache side channels to reconstruct media data. We conduct qualitative and quantitative evaluations of six datasets that represent daily media data whose user privacy can be violated if leaked to adversaries. Our findings show that user inputs can be reconstructed automatically and that the recovered media content, such as images or text, shows considerable (visual) similarity to user inputs. The attention modules facilitate localizing program points that incur input leakage; some have been disclosed before [45, 117, 123], but many, to the best of our knowledge, were previously unknown. Further, we find that perception blinding is highly effective in mitigation of manifold learning–based SCA. We also demonstrate the noise resiliency of our attack, and how oblivious RAM [42, 97] can mitigate our attack, though it incurs high cost and becomes impractical in real-life usage. In summary, this thorough study makes the following contributions:

- Advances in cross-modality manifold learning inspired us to advocate SCA of media software as a supervised task that learns a joint manifold of media data and side channel traces. High-quality media data can be reconstructed from side channel traces in a noise-resilient manner without knowledge of the underlying media software implementation or media data formats.
- We enhance autoencoder with attention to localize program points that make notable contributions to information leakage. Furthermore, we design a low-cost perception-blinding technique that effectively mitigates the proposed SCA exploitation.
- Our evaluation subsumes widely used media software used to process images, audio, and text. We demonstrate that high-quality user inputs in various formats can be reconstructed and that perception blinding predominantly impedes our SCA. Our attention-based error-localization technique confirms some program points that have been reported as vulnerable and flags many previously unknown problems in media software.

To facilitate result verification and future research, we released all code and data generated in this research at [3].

2 Background

We introduce the high-level procedure of launching SCA in which program inputs are assumed confidential. Let a deterministic and terminating program be P. Executing an input $i \in I$ can be modeled as $P : I \to R$, where R denotes the program behavior during the runtime. Although modern computer architectures prohibit attackers from directly recording R and inferring input $i \in I$, attackers can leverage various *side channels*, which map the runtime behavior of R into an adversarial observation O of certain properties (e.g., cache status) in the execution context of P. The attacker's view can be represented as $view : R \to O$, where given side channel observation O, the attackers leverage composite inverse function $(view \circ P)^{-1} : O \to I$ to map O back to input $i \in I$.

Promising progress has been made by logging (high-resolution) side channels such as accessed cache line, cache bank, or page table entries in an automated manner [29, 45, 74, 116, 117]. Nevertheless, reconstruction of i from logged side channels requires attackers to infer the composite inverse function $(view \circ P)^{-1} : O \to I$. Recovery of such mappings requires an in-depth understanding of how program secrets are propagated (i.e., secret information flow), which could require considerable manual efforts [45, 117] or conducting formal analysis [19, 36, 105]. Note that high-resolution side channels (e.g., cache line access) usually contain millions of records, but only a tiny portion o^* is indeed *input-dependent* [104].

SCA on Media Software. Despite the widespread adoption of MLaaS to process users' private data, the SCA of media software has not been thoroughly examined. For instance, media software is commonly used to process X-ray images because it allows cost-efficient disease diagnosis with cloud resources. However, the leakage of such images on the cloud (e.g., via cache-based side channels [73]) involves a high risk of violating patient privacy. An immense demand exists to gain insights into the extent of privacy problems in media software, given its pervasive use in processing private data. Therefore, we examine real-world media software used to process media data such as photos and daily conversations.

Threat Model and Attack Scenarios. This study reconstructs confidential inputs of media software from side channels. We thus reasonably assume that different inputs of targeted media software can induce distinguishable memory access traces. Otherwise, no information regarding inputs would be leaked.

Profiled SCA [23, 47–49, 54, 77] commonly assumes that side channel logs have been prepared for training and data reconstruction. For our scenario, we generally assume a standard *trace-based* attacker. We assume that a trace of system side channel accesses made by the victim software has been

prepared for use. Our evaluated system side channels include cache line, cache bank, and page table entries. The feasibility of logging such fine-grained information has been demonstrated in real-world scenarios [34, 45, 117, 121], and this assumption has been consistently made by many previous works [20, 37, 53, 104, 105, 113]. In this study, we use Intel Pin [76] to log memory access traces and convert them into corresponding side channel traces (see Sec. 5).

We also benchmark userspace-only scenarios where attackers can launch `Prime+Probe` attack [102] to log cache activities when media software is processing a secret input. We use Mastik [119], a micro-architectural side channel toolkit, to launch "out-of-the-box" `Prime+Probe` and log victim's L1I and L1D cache activities. We pin victim process and `spy` process on the same CPU core; see attack details in Sec. 6.4.

Exploiting new side channels is *not* our focus. We demonstrate our attack over commonly-used side channels. This way, our attack is shown as practically approachable, indicating its high impact and threats under real-world scenarios. Unlike previous SCA on media software [45, 117] or on crypto libraries [124], we do *not* require a "white-box" view (i.e., source code) of victim software. We automatically analyze media software *executables* with different input types. As will be discussed in Sec. 6, we launch manifold learning to reconstruct media data with excellent (visual) similarity to user inputs. Many studies have only flagged program points of information leakage with (unscalable) abstract interpretation or symbolic execution [20, 36, 105]. Direct reconstruction of media data is beyond the scope of such formal method-based techniques, and these studies did not propose SCA mitigation.

3 A Manifold View on SCA of Media Software

This study recasts the SCA of media software as a cross-modality manifold learning task that can be well addressed with supervised learning. We train an autoencoder [50] that maps side channel observations O to the media inputs I of media software. Our threat model (Sec. 2) assumes that attackers can profile the target media software and collect side channel traces derived from many inputs. Therefore, our autoencoder framework is trained to learn from historical data and implicitly forms a low-dimensional joint manifold between the side channel logs and media inputs. We first introduce the concept of manifold, which will help to clarify critical design decisions of our framework (see Sec. 4).

Manifold Learning. The use of manifold underlies the feasibility of dimensionality reduction [65]. The key premise of manifold is the *manifold hypothesis*, which states that real-world data in high-dimensional space are concentrated near a low-dimensional manifold [39]. That is, real-world data often lie in a manifold $\mathcal{M}$ of much lower dimensionality d, which is embedded in its high-dimensional space $\mathcal{R}$ of dimensionality D ($d \ll D$). *Manifold learning* aims to find a projection $f : \mathcal{R} \to \mathcal{M}$ that converts data $x \in \mathcal{R}$ into y in an intrinsic coordinate system of $\mathcal{M}$.[1] f^{-1} projects $f(x) \in \mathcal{M}$ back onto representation x in the high-dimensional space $\mathcal{R}$.

PCA [7] is a linear manifold learning algorithm that aims to find $\mathcal{M}$ by extracting "principal components" of data points [15]. However, most real-world manifolds are nonlinear, and manifold learning algorithms (e.g., ISOMAP) are proposed to project data x onto nonlinear $\mathcal{M}$ [12].

Manifold learning views high-dimensional media data $x \in \mathcal{R}$ as a composite of perceptually meaningful contents that are shown as robust to noise or other input perturbations [40, 125, 126]. Manifold learning algorithms extract expressive representations of high-dimensional data such as images, audio, and text [25, 46], which explains why AI models can make accurate predictions pertaining to high-dimensional data [15]. It is shown that data of the same class (e.g., face photos) generally lie in the same manifold, whereas data of different classes (face vs. vehicle photos) are concentrated on separate manifolds in low-dimensional space [100]. manifold learning clarifies the inherent difficulty of designing *universal* encoding and generative models applicable to high-dimensional data from different manifolds. The manifold hypothesis has been verified theoretically and empirically in a comprehensive manner [40, 125, 126]. Appx. A presents our exploration on the validity of manifold hypothesis.

Parametric Manifold. Most manifold learning schemes adopt non-parametric approaches. Despite the simplicity, non-parametric approaches cannot be used to project *new* data points in $\mathcal{R}$ onto $\mathcal{M}$. Recent advances in deep neural networks, particularly autoencoders, have enabled a parametric nonlinear manifold projection $f_\theta : \mathcal{R} \to \mathcal{M}$ [125]. Manifold learning can thus process unknown data points of high-dimensional media data [15, 41, 51, 67, 125, 126] and facilitate downstream tasks like face recognition [39].

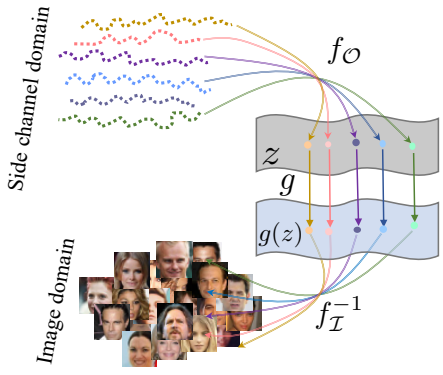


Figure 1: Mapping between side channels and images via a low-dimensional joint manifold $\mathcal{M}_{\mathcal{I},\mathcal{O}} = \mathcal{I} \times \mathcal{O}$.

[1] "Intrinsic coordinate" denotes the coordinate system of the low-dimensional manifold space for each high-dimensional data sample [32, 70].

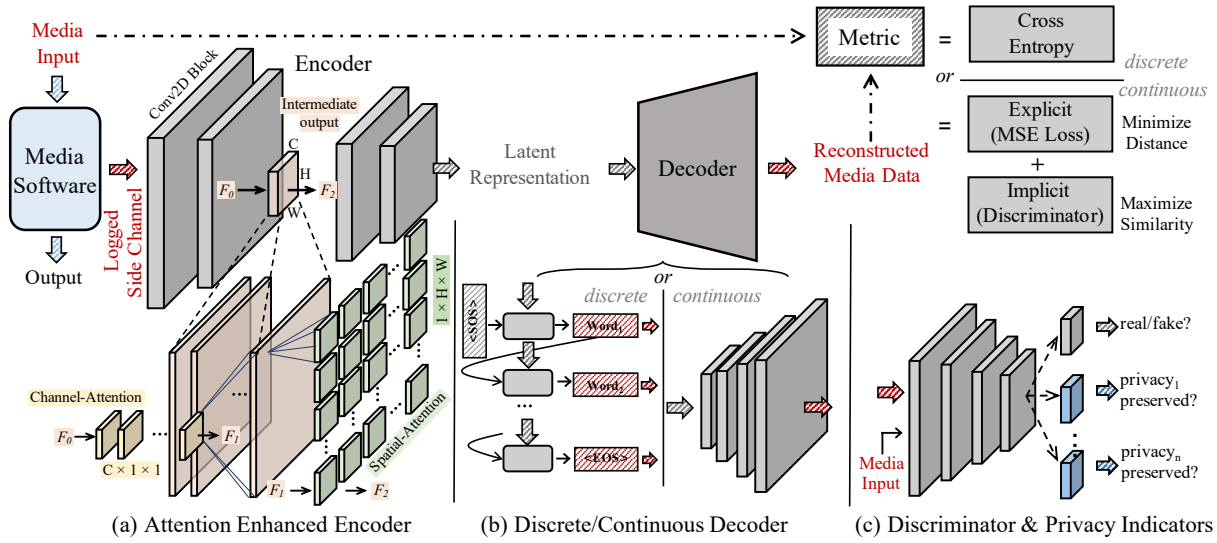


Figure 2: Reconstructing media data of different types with a unified autoencoder framework.

High-Level Research Overview

Processing media data has an observable influence on the underlying computing environment; it thus induces side channel traces that can be logged by attackers to infer private inputs. Previous SCA studies, from a holistic view, attempted to (manually) map side channel logs to *data bytes* in media data (similar to how media software treats media data) [45, 117]; reconstruction of media data in a per-pixel manner is thus error-prone and likely requires expertise and manual efforts.

The success of manifold learning in tasks like image editing and cross-modality reconstruction [125, 126] led us to construct a joint, *perception-level* connection between side channel logs and high-dimensional media inputs.[2] Therefore, instead of deciding value of each byte, reconstructing media data is recast into exploring the manifold of media data that satisfies the perception-level combinatory constraints.

Overall, we view SCA as a cross-modality high-dimensional data reconstruction task that is addressed with joint manifold learning in this work [125]. Aligned with the notations in Sec. 2, let the media software inputs be I; the attacker's observation on executing each input $i \in I$ can be represented as $(view \circ P) : I \to O$, where $o \in O$ denotes the observation of side channel traces. Let F be the composite function $view \circ P$. According to the manifold hypothesis, we assume that I and O also lie in the unknown manifolds $\mathcal{I}$ and $\mathcal{O}$, respectively. As mentioned in our threat model (Sec. 2), we assume that side channel observations depend on the inputs of media software; therefore, the entire joint dataset $\{i_i, o_i\}$ formed by the ith media input $i_i \in I$ and the corresponding ith observation $o_i \in O$ lies in a joint manifold

$$\mathcal{M}_{\mathcal{I},\mathcal{O}} = \{(i, F(i)) | i \in \mathcal{I}, F(i) \in \mathcal{O}\}$$

where $(i, F(i))$ is described with the regular high-dimensional coordinate system. Since I and O also lie in the corresponding manifolds $\mathcal{I}$ and $\mathcal{O}$, the data points in $\mathcal{M}_{\mathcal{I},\mathcal{O}}$ should be equivalently described using an intrinsic coordinate system $(z, g(z))$. Hence, we assume the existence of a homomorphic mapping $(f_{\mathcal{I}}, f_{\mathcal{O}})$ over $(z, g(z))$ such that $z = f_{\mathcal{O}}(o)$ and $g(z) = f_{\mathcal{I}} \circ F^{-1}(o)$. $f_{\mathcal{O}}$ maps side channel observation $\mathcal{O}$ onto the intrinsic coordinate z, whereas $f_{\mathcal{I}}$ maps high-dimensional media data I onto $g(z)$. Note that g denotes the diffeomorphism (i.e., an isomorphism of two manifolds) between the $\mathcal{I}$ and $\mathcal{O}$ manifolds [125]. Hence, instead of computing $F^{-1} = (view \circ P)^{-1} : O \to I$ to map the side channel observation back onto the media inputs, we leverage the joint manifold to constitute the following composite function:

$$F^{-1}(o) = f_{\mathcal{I}}^{-1} \circ g \circ f_{\mathcal{O}}(o) \tag{1}$$

$i \in I$ can thus be reconstructed using the inverse composite function $f_{\mathcal{I}}^{-1} \circ g \circ f_{\mathcal{O}}$ over the joint manifold $\mathcal{M}_{\mathcal{I},\mathcal{O}}$. Fig. 1 provides a summary and presents a schematic view of how I and O of high-dimensional data are mapped via $\mathcal{M}_{\mathcal{I},\mathcal{O}}$.

The feasibility of using neural networks, especially autoencoders, to facilitate parametric manifold learning has been discussed [51, 78, 125, 126]. Accordingly, we train an autoencoder by encoding side channel traces O onto the latent space with encoder ϕ_θ and by generating media data I with decoder ψ_θ from the latent space. Therefore, Eq. 1 can be learned in an end-to-end manner [15, 125]. Holistically, ϕ_θ and ψ_θ cor-

[2] Perception-level connection means constraints on data bytes formed by perceptual contents (e.g., gender, hair style) in media data are extracted from side channels.

respond to $f_{\mathcal{O}}$ and $f_{\mathcal{I}}^{-1}$, respectively, whereas g is implicitly constructed in the encoded latent space.

4 Framework Design

We describe the design of our autoencoder in Sec. 4.1. Sec. 4.2 clarifies the usage of attention to localize code fragments inducing information leakage. Sec. 4.3 introduces perception blinding to mitigate our SCA.

4.1 SCA with Autoencoder

We propose a general and highly-flexible design in which an autoencoder is used to facilitate SCA of various media data, including images, audio and text. The autoencoder framework [50] defines a parametric feature-extracting function f_θ, named *encoder*, that enables the projection of the input x onto a latent vector $h = \phi_\theta(x)$. Similarly, autoencoder frameworks also use ψ_θ as a *decoder* that reconstructs input $\hat{x}$ from a latent vector $\hat{x} = \psi_\theta(h)$. A well-trained autoencoder framework gradually identifies a parameter vector θ to minimize the reconstruction error as follows:

$$L(\theta) = \sum_t L(x_t, \psi_\theta \circ \phi_\theta(x_t))$$

where x_t is a training sample. Minimal errors can be found with statistical methods like stochastic gradient descent.

The first row of Fig. 2 depicts the workflow. We clarify that our focus is *not* to propose novel model architectures; rather, we show that high-quality inputs can be synthesized by assembling standard models, which indicates severity and effectiveness of our attack. We now discuss the high-level workflow and present the model structures and training details in Sec. 5.1. Given a logged side channel trace $o \in O$, encoder $\phi_\theta(o)$ converts o into the corresponding latent representation. We prepare three decoders ψ_θ^i, ψ_θ^a, ψ_θ^t to reconstruct these types of media data (i.e., image, audio, and text) from the encoded latent representation. We pair encoder $\phi_\theta(o)$ with each ψ_θ^* and train the assembled pipeline for our customized objective functions $L(\theta)$. Our proposed framework is task-agnostic. Generating media data of various types requires only assembling corresponding decoders to the unified encoder ϕ_θ.

Encoder ϕ_θ. A logged side channel trace will first be folded into a $K \times N \times N$ matrix (see Table 3 for the detailed configuration of each trace). We then feed this matrix as the input of encoder ϕ_θ. The encoder ϕ_θ comprises several stacked 2D convolutional neural networks (CNNs). For the current implementation, ϕ_θ converts the high-dimensional inputs into latent vectors of 128 dimensions, given that the dimensions of our media inputs are all over 10K. See Appx. F for clarification on how side channels, including both Intel Pin- and `Prime+Probe`-logged records, are represented and processed by ϕ_θ. Moreover, we find that increasing the dimension of latent vectors (i.e., from 128 to 256) does not make an observable improvement. This observation is consistent with the manifold hypothesis [65], such that only *limited* "perceptions" exist in normal media data. In contrast, reducing the number of dimensions (e.g., 32) makes the outputs (visually) much worse. However, users who strive to recover media data of lower-dimensions can configure our framework with smaller latent vectors (e.g., 32 dimensions).

Fig. 2(a) shows that we enhance encoder ϕ_θ with attention. Indeed, we insert one attention module between every two stacked CNN layers in the encoder. Attention generally improves output quality of autoencoder [103]. More importantly, attention facilitates localizing program points of information leakage. We elaborate on Fig. 2(a) in Sec. 4.2.

Decoder ψ_θ^*. We categorize the media data exploited by this study into two types: continuous and discrete. Image and audio data are represented as a continuous floating-point matrix and reconstructed by ψ_θ^i and ψ_θ^a in a continuous manner. In contrast, textual data comprise word sequences, and because there is no "intermediate word," textual data are regarded as sequences of discrete values and handled by ψ_θ^t.

As shown in Fig. 2(b), we use a common approach to stacking 2D CNNs to design ψ_θ^i. A 2D CNN has several convolutional kernels; each kernel focuses on one feature dimension of its input and captures the spatial information of this feature dimension. Images can thus be reconstructed from vectors in the low-dimensional latent space with stacked 2D CNNs, as each 2D CNN upsamples from the output of the previous layer. For audio data, we first convert raw audio into the log-amplitude of Mel spectrum (LMS), a common 2D representation of audio data. As will be shown in Fig. 20, audio data are represented as 2D images, in which the x-axis denotes time and the y-axis denotes the log scale of amplitudes at different frequencies. Herein, like ψ_θ^i, ψ_θ^a uses stacked 2D CNNs to process each converted 2D image, gradually upsamples from the latent representation, and reconstruct the LMSs of the audio data. Because the LMSs usually are not in square-shape, we append a fully connected layer to transform the shape of the reconstructed LMSs. These LMSs are then converted to raw audio losslessly.

Textual data, however, are reconstructed sequentially "word by word" due to their discrete nature. As shown in Fig. 2(b), to reconstruct a sentence from the latent space of a side channel trace o, a single word is gradually inferred based on words already inferred from sentence i. Following a common practice of training sequence-to-sequence autoencoders, we add a start-of-sequence (SOS) token before each sentence i and an end-of-sequence (EOS) token after i. Then, given a side channel trace o that corresponds to unknown text i, the trained decoder ψ_θ^t starts from the SOS token and predicts a word $w \in i$ sequentially until it yields the EOS token. From a holistic perspective, the trained model projects a sentence i into a low-dimensional manifold space of *word dependency*, which facilitates the gradual inference of each word w on i.

Table 1: Privacy-aware indicators. Table 3 introduces each dataset.

Dataset	Indicator
CelebA	Is the celebrity's identity preserved?
ChestX-ray	Is the disease information preserved?
SC09	Is the speaker's identity preserved?
Sub-URMP	Is the musical instrument's type preserved?

Designing Objective Functions. As depicted in the first row of Fig. 2, for discrete data (i.e., text), each decode step is a multi-class classification task where the output is classified as one element in a pre-defined dictionary. Thus, we use *cross entropy* as the training objective. For continuous data, we design the training objective L_θ *composing both explicit and implicit metrics*. We now introduce each component in detail.

Explicit Metrics A common practice in training an autoencoder is to explicitly assess the point-wise distance between the reconstructed media input i' and reference input i with metrics such as MSE loss, L1 loss, and KL divergence [28,60]. The autoencoder will be guided to gradually minimize the point-wise distance $L_\theta(i, \psi_\theta \circ \phi_\theta(o))$ during training. Nevertheless, a major drawback of such explicit metrics is that the loss of each data point is calculated *independently* and contributes *equally* to update θ and minimize L_θ. Our preliminary study (see Fig. 25 in Appx. G) shows that such explicit metrics suffer from "over-smoothing" [90], a well-known problem that leads to quality degradation of the reconstructed data.

Implicit Metrics Another popular approach is to assess the "distributed similarity" [90] of reconstructed i' and reference input i. Viewing the general difficulty of extracting the distribution of arbitrary media data, a common practice is to leverage a neural discriminator D. Discriminator D and decoder ψ_θ play a zero-sum game, in which D aims to distinguish the reconstructed input i' from normal media data i. In contrast, decoder ψ_θ tries to make its output i' indistinguishable with i to fool D. Although this paradigm generally alleviates the obstacle of "over-smoothing" [90], it creates the new challenge of mode collapse; that is, ψ_θ generates realistic (albeit very limited) i' from any inference inputs. From a holistic perspective, the use of a discriminator mainly ensures that the reconstructed i' is near i from a *distribution* perspective; no guarantee is provided from the view of a single data point.

Privacy-Aware Indicators In addition to the two standard objective functions mentioned above, we further take into account a set of *privacy-aware indicators*. As shown in Fig. 2(c), we extend discriminator D such that it checks whether the reconstructed outputs preserve the "privacy" in an explicit manner. Table 1 lists the privacy indicators used in our framework, which correspond to exploited media data of different types. For instance, for face photos (CelebA), we specify checking the identity. Hence, the enhanced discriminator D serves as a classifier to check whether the identity of the person is preserved, which thus forces decoder ψ_θ to decode the identity information in the zero-sum game. A specific fully connected layer is appended to the discriminator D in accordance with each privacy indicator.

Comparison with Generative Model-Based SCA [123]. One contemporary study [123] uses generative models (e.g., GANs [44]) to conduct SCA towards image libraries by capturing image distribution from side channels. Nevertheless, their work is particularly designed to recover images instead of proposing a general and flexible framework to exploit media software of various input types. In addition, we explicitly use privacy indicators when designing objective functions, while [123] focuses on polishing the *visual appearance* of the reconstructed images.

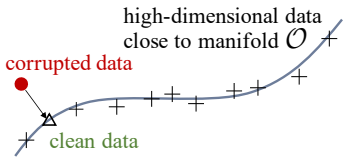


Figure 3: Denoising corrupted data during manifold learning.

Noisy Side Channel. Reconstructing media data from noisy side channels is of particular importance, because adversaries often face considerable noise in real-world attack scenarios. Manifold learning features denoising by design, the schematic view of which is presented in Fig. 3. Overall, manifold learning forces side channel traces O to concentrate near the learned low-dimensional manifold $\mathcal{O}$, where a corrupted high-dimensional data point $\tilde{o}$ (● in Fig. 3) should typically remain *orthogonal* to the manifold $\mathcal{O}$ [15]. Thus, when the decoder ψ_θ learns to reconstruct media data $i \in I$ from the representations lying on the joint manifold, corrupted $\tilde{o}$ can be fixed by first being projected onto the Δ in the manifold for denoising; and i can then be reconstructed from the Δ [51].

4.2 Fault Localization with Neural Attention

Some studies have detected software vulnerabilities that lead to side channel attacks [19, 36, 104, 105]. However, we note that such studies typically use heavyweight program-analysis techniques, such as abstract interpretation, symbolic execution, and constraint solving. Thus, performing scalable program analysis of real-world media software could prove a great challenge, given that such media software usually contains complex program structures (e.g., nested loops) and a large code base. Furthermore, the primary focus of previous studies has been crypto libraries (e.g., OpenSSL [82]), whose "sensitive data" are private key bytes or random numbers. In contrast, modeling potentially lengthy media data with various strictly defined formats could impose a further challenge (e.g., symbolizing such complex input formats) that may require the incorporation of domain-specific knowledge.

Inspired by advances in program neural smoothing [94, 95] and SCA based on neural networks [54, 85, 118, 123], we seek to overcome question "which program point leaks side channel information" by answering the following question:

> "Which records on a logged side channel trace contribute most to the reconstruction of media data?"[3]

Although answering the former question often requires rigorous and unscalable static analysis, the second question can be addressed smoothly by extending the encoder ϕ_θ with *attention* [114], a well-established mechanism that improves the representation of interest by telling the neural network where and upon what to focus. In particular, by enhancing the autoencoder with attention, our framework *automatically* flags side channel logs that make a primary contribution to input reconstruction. These logs are *automatically* mapped to the corresponding memory access instructions. We can then *manually* identify the corresponding "buggy" source code. For the last step, our current experiments rely on symbol information in the assembly programs to first identify corresponding functions in source code, and then narrow down to code fragments inducing input leakage.

Despite attention being a standard mechanism to boost deep learning models [103, 114], attention in our new scenario acts like a "bug detector" to principally ease localizing vulnerable program points. In contrast to program analysis-based approaches [19, 36, 104, 105], our solution is highly scalable and incurs no extra cost during exploitation. Moreover, it analyzes software in a black-box setting that is agnostic to media software implementation details or input formats.

Fig. 2(a) depicts the enhanced trace encoder with attention. An attention module (we follow the design in [114] given its simplicity and efficiency) is inserted within every two stacked CNN layers. Let the intermediate input of a CNN layer as $C \times H \times W$, the "Channel-Attention" module $A_{channel}$ processes each segment of $1 \times H \times W$ data points from C channels and tells the encoder "where" to focus on by assigning different weights to each segment. The "Spatial-Attention" module $A_{spatial}$ processes each segment of $C \times 1 \times 1$ records and advises the encoder "what to locate" by assigning different weight on each record. From a holistic perspective, attention module $A_{channel}$ projects a coarse-grained focus on potentially interesting segments, while $A_{spatial}$ further identifies interesting side channel records in a segment.[4]

4.3 Mitigation with Perception Blinding

This section presents mitigation against manifold learning–enabled SCA (Sec. 4.1). Consistent with our attack and fault-localization, mitigation is also agnostic to particular media software and input types. We only need perturb the media input I with pre-defined perception blinding masks.

We first introduce blinding images of the human face, and then explain how to extend perception blinding toward other input types. Appx. B presents the workflow of perception blinding in real systems and discusses application scope.

A Working Example. As introduced in Sec. 2, manifold learning casts images of the human face into a set of perceptually meaningful representations; typical representations include hair style, age, and skin color. Hence, we define a *universal* mask i_{mask} of human face, such that by perturbing arbitrary images i of human face with i_{mask}, the produced output $i_{blinded}$ will be primarily projected to the same intrinsic coordinates z_{mask} in the manifold space $\mathcal{M}$. To use perception blinding, users only need to pick *one* mask i_{mask} to blind all input images i. Consequently, adversaries are restricted to the generation of media data perceptually correlated to z_{mask}. Particularly, to perturb i, we add i_{mask} as follows:

$$i_{blinded} = \alpha \times i \oplus \beta \times i_{mask}$$

where we require $\beta \gg \alpha$ and $\alpha + \beta = 1$. Perceptual contents of i_{mask} thus "dominates" the projected low-dimensional perceptions in $\mathcal{M}$. Let $P(i_{blinded})$ be the output of media software after processing $i_{blinded}$, and the user can recover the desired output by subtracting $P(i_{mask})$ from the output as follows:

$$P(i_{private}) = \frac{1}{\alpha} \times (P(i_{blinded}) \ominus \beta \times P(i_{mask}))$$

where $P(i_{private})$ is the desired output, and $P(i_{mask})$ can be precomputed. $\oplus$ and $\ominus$ directly operate $i \in I$ of various formats, as will be defined later in this section. Because typical operations of media software (e.g., compression) are *independent* of the perceptual meaning of media inputs, the proposed blinding scheme introduces no extra hurdle for media software. In contrast, as shown in Sec. 6.3, SCA based on manifold learning can be mitigated in a highly effective manner.

Requirement of i_{mask}. Comparable to how RSA blinding is used to mitigate timing channels [21], perception blinding is specifically designed to mitigate manifold learning-based SCA. We require that i_{mask} must lie in the same low-dimensional manifold with the private data. Thus, i_{mask} must manifest high **perception correlation** with media software inputs $i_{private} \in I$. This shall generally ensure two properties: 1) the privacy (in terms of certain perceptions, such as gender and skin color) in $i_{private}$ can be successfully "covered" by i_{mask}, and 2) i_{mask} imposes nearly no information loss on recovering $P(i_{private})$ from $P(i_{blinded})$ except a mild computational cost due to mask operations. Considering Fig. 3, when violating this requirement of *perception correlation*, for instance, such as by using random noise to craft i_{mask}, the intrinsic coordinate of the original input (Δ) can likely drift to

[3] See Appx. F for trace representation.

[4] It is well accepted that a CNN is organized in the form of `num_channels` × `width` × `height`. Therefore, we name two attention components as $A_{channel}$ and $A_{spatial}$, which are aligned with the convention.

Table 2: Side channels derived from a memory access made by victim media software using address *addr*.

Side Channel Name	Side Channel Record Calculation
CPU Cache Bank Index [121]	$addr \gg L$ where L, denoting cache bank size, is usually 2 on modern computer architectures.
CPU Cache Line Index	$addr \gg L$ where L, denoting cache line size, is usually 6 on modern computer architectures.
OS Page Table Index [45, 120]	$addr \,\&\, (\sim M)$ where M, denoting `PAGE_MASK`, is usually 4095 on modern computer architectures.

Table 3: Statistics of side channel traces and media software. There is *no* overlapping between training and testing data.

Dataset	Information	Training Split	Testing Split	Trace Length	Matrix Encoding	Media Software
CelebA [75]	Large-scale celebrity face photos	162,770	19,962	$338,123 \pm 14,264$	$6 \times 256 \times 256$	`libjpeg` (ver. 2.0.6)
ChestX-ray [106]	Hospital-scale chest X-ray images	86,524	25,596	$329,155 \pm 10,186$	$6 \times 256 \times 256$	LOC: 103,273
SC09 [111]	Human voice of saying number 0–9	18,620	2,552	$1,835,067 \pm 103,328$	$8 \times 512 \times 512$	`ffmpeg` (ver. 4.3)
Sub-URMP [66]	Sound clips of 13 instruments	71,230	9,575	$1,678,485 \pm 36,122$	$8 \times 512 \times 512$	LOC: 1,236,079
COCO [71]	Image captions	414,113	202,654	$77,796 \pm 14$	$6 \times 128 \times 128$	`hunspell` (vers. 1.7.0)
DailyDialog [68]	Sentences of daily chats	11,118	1,000	$77,799 \pm 102$	$6 \times 128 \times 128$	LOC: 39,096

a "corrupted input" (●) that is mostly orthogonal to the manifold of I. As explained in Sec. 4.1, due to the inherent noise resilience of manifold learning, crafting such a corrupted input can cause less challenge to attackers when recovering i from the low-level manifold space. Although $i_{private}$ is of low weight in $i_{blinded}$, it can still be reconstructed to some extent, as will be shown in Fig. 7 of Sec. 6.3.

Extension to other data types. For image and audio data, we recommend using a normal image $i \in I$ as the mask i_{mask}. Intuitively, by amplifying i_{mask} with a large coefficient β in generating $i_{blinded}$, i_{mask} is presumed to dominate the perceptual features in $i_{private}$. Hence, we stealthily hide the private perceptual features of $i_{private}$ in $i_{blinded}$, whose contents are difficult for adversaries to disentangle without knowing i_{mask}. For textual data, we recommend inserting notional words of high frequency to blind $i_{private}$. We present empirical results on how various choices of i_{mask} can influence the mitigation effectiveness in Sec. 6.3.

Implementation of Operators $\oplus$ And $\ominus$. For image and audio data, we use floating-point number addition and subtraction to implement $\oplus$ and $\ominus$. Textual data are discrete: considering that media software often manipulates textual data at the word level, simply "adding" or altering words in the input text will likely trigger some error handling routines of the corresponding media software, which is not desirable. Sec. 4.1 clarifies that our autoencoder framework essentially captures the "word dependency" between words in a sentence; accordingly, we define the $\oplus$ operation as inserting words in a sentence, whereas the $\ominus$ operation is implemented to remove previously inserted words. As shown in Sec. 6.3, this strategy effectively breaks the word dependency in the original text.

5 Attack Setup

We leverage three high-resolution side channels, as shown in Table 2. As clarified in our threat model (Sec. 2), these side channel are commonly adopted in previous works. See Appx. C for detailed setup of these side channels. We clarify that exploiting new side channels is *not* our focus. We use common side channels in the era of cloud computing, implying the severity and effectiveness of our proposed attack. The resolution when performing attacks on those side channels are 4B, 64B, and 4096B, respectively. Higher-resolution side channels should enable recovering media data with more vivid details. Media data of better quality, however, does not necessarily enhance privacy stealing (e.g., determining whether chest X-Ray images indicate pneumonia). See quantitative evaluation of privacy inference in Sec. 6.1.2.

For evaluation in Sec. 6, we use `Pin` [76] to collect memory access traces and map each trace into three side channel traces following mapping rules in Table 2. Sec. 6.4 further demonstrates attack in an userspace-only scenario, i.e., we collect cache side channels via `Prime+Probe` [102].

Media Software and Media Dataset. Table 3 reports evaluated media software and statistics of side channel traces. We pick media software consistent with previous works [45, 117, 123]. All media software are complex real-world software, e.g., `FFmpeg` contains 1M LOC. In contrast, crypto libraries are usually much succinct, e.g., x86 core implementation of AES in recent `OpenSSL` has about 3K LOC. We prepare two common datasets for each media software to comprehensively evaluate our attack. All datasets contain daily media data that, once exposed to adversaries, would result in privacy leakage. We compile all three media software into 64-bit binary code using `gcc` on a 64-bit Ubuntu 18.04 machine. See Appx. C for details of these software and datasets.

5.1 Implementation

We implement our framework in Pytorch (ver. 1.4.0). We use the Adam optimizer with learning rate as 0.0002 for all models. Batch size is 64. For continuous decoders, we set the loss function as $\lambda L_{exlicit} + L_{implicit} + \sum_{i=1}^{n} L_{privacy}$, where $\lambda = 50$ and n is the number of privacy-aware indicators. We ran experiments on Intel Xeon CPU E5-2683 with 256 GB RAM and one Nvidia GeForce RTX 2080 GPU. For experiments based on `Prime+Probe`-logged traces (Table 3), the training

Table 4: CelebA face image matching evaluation.

	Cache bank	Cache line	Page table
same face	45.4%	43.5%	44.5%
non-face	2.0%	2.0%	2.1%

Table 5: SC09 human voice matching evaluation.

	Cache bank	Cache line	Page table
ID accuracy	29.1%	28.8%	23.2%
Content accuracy	21.6%	24.2%	22.6%

is completed at 100 epochs and takes less than 24 hours. For experiments using `Prime+Probe`-logged traces, training and takes shorter time (see **Running Time** in Appx. D). Table 3 reports the dataset size and training/testing splits. See our released codebase [3] for result verification.

6 Evaluation

We present the SCA exploitation toward media software in Sec. 6.1. We discuss program points that induce information leakage in Sec. 6.2, and demonstrate the effectiveness of perception blinding in Sec. 6.3.

6.1 Side Channel Attack

This section reports evaluation results of our attack. Due to the limited space, some setups are reported in Appx. C. We present more evaluation results in Appx. G.

6.1.1 Qualitative Evaluation

This section presents and compares the reconstructed media data with the reference inputs in terms of various settings. Fig. 5 demonstrates that the reconstructed images and the references show highly aligned visual appearances, including gender, eyebrow shapes, skin color, and hair styles. Images constructed from different side channels manifest comparable visual quality. Fig. 4 further reports the text reconstruction results of daily dialogs by comparison with the reference inputs. The reconstructed sentences, although are not fully aligned with the reference, still retain considerable correct contents and the original intents.

We interpret the overall qualitative evaluation results, in terms of images and text, as highly encouraging. We present reconstructed chest X-ray images, sub-URMP/SC09 audio data, and COCO text in Appx. G. Promising results can be consistently observed.

6.1.2 Quantitative Evaluation

Image Data. For CelebA, we leverage commercial face recognition APIs, Face++ [5], to decide whether a reconstructed face and its reference input can be considered as from the *same person* with over 99.9% confidence scores. We thus launch a de-anonymization attack of user identity with reconstructed images. Table 4 reports the evaluation results; for all three exploited side channels, more than 43% of the reconstructed faces can be correctly matched to their reference inputs, showing a high success rate of face matching. Only 2% of the reconstructed images are deemed as "non-face," which indicates the negligible chance of generating corrupted faces. Due to the limited space, we report the quantitative evaluation of chest X-ray in Appx. G.

Table 6: Text data inference evaluation.

Dataset	Cache bank	Cache line	Page table	Baseline
COCO Caption	43.4%	42.6%	42.1%	0.0000%
Daily Diolgue	38.1%	37.4%	37.6%	0.0183%

Our attack achieves plausible accuracy. The quantitative results are *not* noticeably affected by differences in side channels, which indicates that face matching evaluation extracts representative attributes from images for matching. As mentioned in Sec. 5, the three side channels manifest different resolutions: although higher-resolution side channels enable reconstruction of more vivid images, this does not necessarily promote privacy stealing. However, enabled by manifold learning-based autoencoder and our objective functions which explicitly account for privacy indicators (Table 1), privacy-related factors are extracted in the reconstructed images across side channels of various resolutions. Similar observations are made for media data of other formats; our discussion follows.

Audio Data. Table 5 reports the voice matching results for SC09. Using the reconstructed voice commands (number 0–9), we train two classifiers for speaker identity and command 0–9 classification.[5] The evaluation results largely outperform the baseline (i.e., random guessing). With a total of 184 speakers, we achieve greater than 20% accuracy in matching correct speaker identities across all settings. We also exceed 20% accuracy in content matching (0–9). We observed decreasing accuracy in speaker identity matching, which is reasonable given that the cache bank side channel only "kicks off" two least significant bits, while cache line and page table side channels retain less amount of information. Appx. G reports the matching rate of musical instruments in Table 16, which yields mostly consistent and promising findings.

Text Data. To reconstruct text data, we gradually predict each word based on previously-predicted words in the sentence. Hence, for the quantitative evaluation, we adopt an attack strategy mostly aligned with [24] to measure the average accuracy of word-level prediction accuracy. Table 6 reports the evaluation results for the COCO and Dailydialog datasets. To prepare a baseline for comparison, we feed a random input to the decoder ψ_θ instead of using the latent vector of an input side channel trace. As expected, our exploitation of both

[5] Please refer to Appx. C for details of these classifiers.

Reconstructed Text	Reference Input
*I think it **' be better for find** a good babysitter here . It **' be cost , an** or three days .*	*I think it would be better to have a good babysitter here . It might even be for two or three days .*
*She **is** a **single** cold , and **it** don ' t want to take **care to** us . But we don ' t like **how** can stay with our .*	*She has a bad cold , and we don ' t want to take her with us . But we don ' t know who can stay with her .*
*I ' m sorry **, say that** . What ' s wrong with her ?*	*I ' m sorry to hear it . What ' s wrong with her ?*

Figure 4: Qualitative evaluation of DailyDialog. We mark ***inconsistent reconstructions***.



Figure 5: Qualitative evaluation of CelebA.

```
1  static void idct32(int *coeffs, int col_limit) {
2    int limit = min(H, col_limit + 4);
3    for (int i = 0; i < H; i++)
4      TR_32(src, src, H, H, limit);
5  }
6  static void TR_32(int *dst, int *src, int dstep,
7                    int sstep, int end) {
8    int o_32[16] = { 0 };
9    for (int i = 0; i < 16; i++)
10     // loading pre-calculated matrix ''transform''
11     for (int j = 1; j < end; j += 2)
12       o_32[i] += transform[j][i] * src[j * sstep];
13   // TR_16 calls TR_8, and TR_8 calls TR_4.
14   TR_16(e_32, src, 1, 2 * sstep, SET, end/2);
15 }
```

Figure 6: Vulnerable code components in `FFmpeg`. We mark variables depending on `FFmpeg`'s input in red, and **bold** input-dependent memory accesses (line 12).

Table 7: Localized program points in `libjpeg`.

Module	#Functions	Frequency	Sample Func. Names
MCU	2	7,060	`encode_mcu_huff` `decode_mcu`
Transform	1	5866	`jtransform_execute_transform`
IDCT	13	4,027	`jpeg_idct_15x15` `jsimd_idct_ifas`
Upsample	15	2,033	`h2v1_merged_upsample` `h2v1_fancy_upsample`
Decompress	6	1,352	`tjDecompress2` `tjDecompressHeader3`
Dump	4	8,23	`write_bmp_header` `start_input_bmp`

Table 8: Localized program points in `FFmpeg`.

Module	#Functions	Frequency	Sample Func. Names
Encode	50+	10K+	`encode_frame`
Decode	50+	10K+	`decode_frame`
Filter	50+	10K+	`filter_frame`
IDCT	10+	5K+	`idct_idct_32x32_add_ce` `iadst_idct_16x16_add_c`
Dump	10+	5K+	`wav_write_trailer` `wav_write_header`

datasets achieves much greater accuracy than the baseline regarding all side channels.

6.2 Program Point Localization

We now discuss the localized buggy code of each media software using attention. We present a representative buggy code fragment of `FFmpeg` in Fig. 6. We further present representative buggy code fragments of `libjpeg` and `Hunspell` in Appx. G. We also list **all** localized program points in term of assembly code in [3].

`libjpeg`. We analyze 2,000 media inputs from the CelebA and Chest X-ray datasets. Table 7 reports the localization results of `libjpeg`. For instance, we identify 7,060 side channel points from 4,000 traces, which can be mapped back to two functions (`encode_mcu_huff` and `decode_mcu`) performing minimum coded unit (MCU)-related operations. Similarly, we find information leakage points in modules related to decompression, IDCT, and also output dumping.

Table 3 shows that *one* trace has approximately 400K data points. In other words, Table 7 reveals that a tiny portion of "informative" points on a side channel trace make a primary contribution to information reconstruction. Given an image compressed in JPEG, `libjpeg` decompresses the image into a bitmap. It is pointed out that the decompression process introduces side channels. IDCT-related functions that were noted by [117] are automatically re-discovered by us. In addition, we identify functions in other image transformation routines (e.g., MCU, unsampling) and output dumping routines that leak inputs. We manually inspected the corresponding implementation of `libjpeg` and confirmed our findings. Note

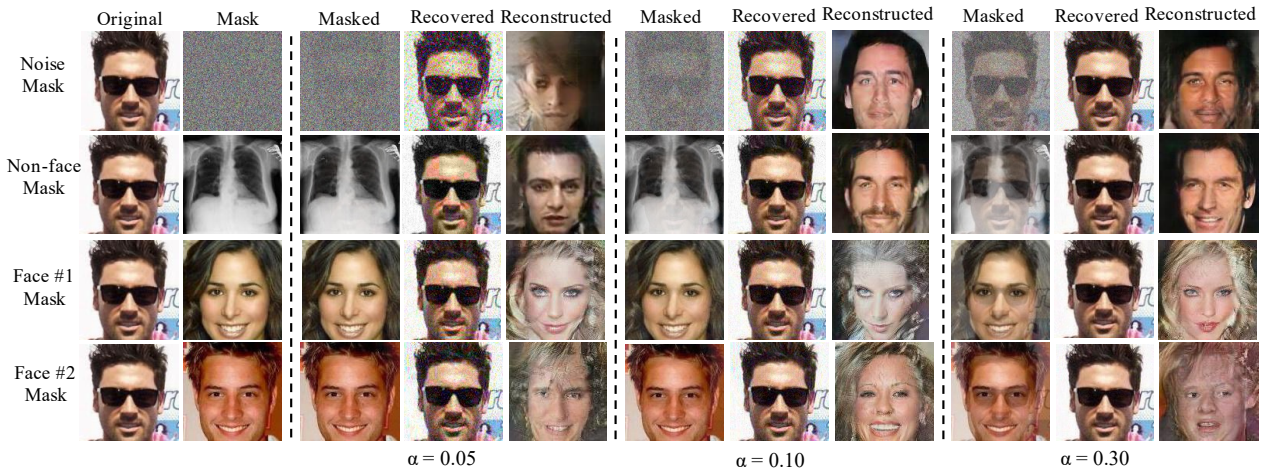


Figure 7: Qualitative evaluation results of perception blinding.

Table 9: Localized program points in `Hunspell`.

Module	#Functions	Frequency	Sample Func. Names
Interface	1	1,333	`pipe_interface`
Parser	4	1,230	`next_token`, `alloc_token` `get_parser`, `TextParser::init`
Look up	2	213	`check`, `insertion_sort`
Insert	5	1,076	`putdic`, `allocate_string` `chenc`, `allocate_char_vector`

that our approach is automated and treats the entire `libjpeg` software as a blackbox, whereas previous studies [45, 64, 117] could rely on expert knowledge to first localize the vulnerable program points before launching SCA.

`FFmpeg`. We use 2,000 inputs from SC09 and Sub-URMP as the inputs of `FFmpeg`. Our findings, as reported in Table 8, can be mapped to five modules of `FFmpeg`, each of which contains many functions. `FFmpeg` processes audio inputs with audio sampling (the sampling frequency is set as 4,000 in our experiments). Fig. 6 presents a vulnerable program component in the IDCT module of `FFmpeg` where the input "taints" certain variables (marked in red) and eventually influences the memory accesses at line 12. Given different input values, different memory cells are visited at line 12, resulting in access to different cache units or page table entries. In addition, `TR_32`, `TR_8` and `TR_4` also suffer from similar patterns (line 14). To the best of our knowledge, side channel issues on `FFmpeg` are rarely studied, but the findings in `FFmpeg` are conceptually similar to other media software; for example, IDCT algorithms and output dumping in both `FFmpeg` and `libjpeg` are flagged as vulnerable by us.

`Hunspell`. We use 2,000 inputs from each dataset (i.e., DailyDialog and COCO) to run `Hunspell` and analyze the logged side channels. Table 9 reports the results, where information leakage points are found from the interface, parser, and also spell checking . In fact, previous works [64, 117] have pointed out side channel issues of `Hunspell`. `Hunspell` performs spell check, where a dictionary of words is maintained as a hash table. `Hunspell` iterates each word w in the input sentence to check if w is in the hash table, thus deciding the correctness of its spelling. When checking each w, `Hunspell` computes the hash value of w and looks up the corresponding hash bucket of words. This would lead to a sequence of memory accesses, which can be potentially used to map back to word w. Note that while previous works attacking `Hunspell` assumes the knowledge of the dictionary [64, 117] before attack, such pre-knowledge is *not* needed for our attack. Instead, we use side channel traces and their corresponding sentences fed to `Hunspell` as the training data to implicitly learn a mapping in the low-dimensional joint manifold space. [64, 117] reports that functions `lookup` and `add_word` primarily leak inputs. Our manual confirmation shows that our findings (e.g., `putdic`, `chenc`, `check`, `insertion_sort`) indeed invoke `lookup` and `add_word` functions. We also find that the parser and interface (we use Linux utility `echo` to feed `Hunspell`) of `Hunspell` also influence side channels, both of which are not disclosed by previous works.

Confirmation with the Developers. We have reported our localized program points to the developers. By the time of writing, the FFmpeg developers confirmed our findings. Nevertheless, they mentioned that software-level fixing is undesirable, given the difficulty of writing side channel-free code and the incurred extra performance penalty. From his perspective, OS-level or hardware-level fixing seems more practical.

6.3 Mitigation with Perception Blinding

We benchmark the mitigation effectiveness in terms of quantitative and qualitative analysis. We also discuss how different masks can influence the mitigation.

Table 10: Face matching results after blinding in terms of (cache bank/cache line/page table).

Mask	$\alpha = 0.05$	$\alpha = 0.1$	$\alpha = 0.3$
Noise	27.5/28.6/27.8%	25.2/26.9/28.2%	26.6/27.5/29.0%
Non-face	28.8/28.8/26.5%	26.2/27.6/27.4%	28.7/31.4/26.2%
Face#1	1.4/1.2/2.4%	1.8/1.4/2.7%	2.0/1.5/3.1%
Face#2	0.6/1.3/1.6%	0.7/1.7/1.9%	1.2/1.6/2.2%

Table 11: Mitigating COCO text inference attack in terms of (cache bank/cache line/page table). $\alpha = 0.05$, $\alpha = 0.1$, $\alpha = 0.3$ denote each word are appended with 19, 9, and 2 masks, respectively.

Mask	$\alpha = 0.05$	$\alpha = 0.1$	$\alpha = 0.3$
"man"	0.39/0.40/0.36%	0.68/0.69/0.67%	2.46/2.45/2.13%
"sitting"	0.16/0.16/0.22%	0.30/0.30/0.39%	1.36/1.40/1.39%

6.3.1 Qualitative Evaluation

We report qualitative evaluation by comparing the reference inputs with the reconstructed inputs after applying blinding. Due to the limited space, Fig. 7 only reports the perception blinding over a private face image $i_{private}$ in terms of different settings. The original image $i_{private}$ is presented in the "Original" column, and applied perception masks are presented in the "Mask" column. For each masked image $i_{blinded}$, the adversarial recovered images are presented in the "Reconstructed" columns, and the final media software outputs after unblinding are given in the "Recovered" columns.

"Noise mask" (the first row) and "non-face mask" (the second row) do not seem helpful in blinding $i_{private}$ because features such as face orientation are still preserved in the reconstructed images. However, the use of real face images as the mask, as shown in the third and fourth columns, gives promising results to blind key perceptual-level contents like hair color and skin color. Overall, after blinding, the adversary-reconstructed images seem to show a correlation with i_{mask} instead of $i_{private}$. This is intuitive; as clarified in Sec. 4.3, a large coefficient β is assigned to i_{mask} such that the perception contents of i_{mask} largely determine the projected intrinsic coordinate in the manifold. This way, the reconstructed images incline to manifest the perception of i_{mask}.

Additionally, although a small α value (e.g., 0.05) introduces a non-trivial amount of noise in the final output, outputs of much better quality can be recovered when α is set to 0.10 or even higher. We thus recommend that users adopt a reasonably high α when constituting $i_{blinded}$. More reconstructed cases are given in Appx. H.

6.3.2 Quantitative Evaluation

We launch quantitative evaluation following the procedures in Sec. 6.1. The perception blinding of "Noise" and "Non-face" masks, as shown in Table 10, reduces the average success rates of face matching from approximately 44% (Table 4) to 27.4%, but still has non-negligible privacy leakage. Compared with "Face#1" and "Face#2", Fig. 7 shows that images reconstructed from "Noise"- and "Non-face"-blinded images manifest better visual similarity with the reference inputs. In addition, Table 10 reports that "Face#1" and "Face#2" exhibit much better mitigation (less than 3.1% matching rates) in terms of quantitative metrics. We find that the value of α does *not* notably influence the results but is still positively correlated with privacy leakage. Overall, for images, we mask the perception contents using blinding. However, the privacy indicator for this scenario, i.e., celebrity's identity, is *not* simply a linear sum of all perception contents. Overall, identity recognition depends on subtle features of a human face: changing α not necessarily impedes capturing informative features.

Table 11 reports the mitigation results of `Hunspell` using COCO. We use two notional words of high frequency, "man" and "sitting", for blinding. We insert N notional words after each word in an input sentence, where N ($\frac{1}{\alpha} - 1$) is 19, 9, and 2 given different α. When more notional words are used, we observe a higher decrease in inference accuracy. However, with blinding, the inference accuracy decreases from more than 40.0% (see Table 6) to less than 2.5% (close to baseline; see Table 6) even two notional words are inserted after each normal word. Different from masking images, the privacy of text is assessed by word dependency (introduced in Sec. 6.1.2). α decides #notional words inserted to break word dependency. Therefore, the results changes notably w.r.t. values of α.

In sum, our quantitative evaluation demonstrates the effectiveness of our proposed mitigation despite differences in the media data formats or exploited side channels. See Appendix H for more results; for instance, blinding chest X-ray images can drastically reduce the disease diagnosis F1 score from an average of 0.73 (see Table 17) to less than 0.1.

6.4 Real-World Attack with `Prime+Probe`

This section explores collecting cache access traces via a practical cache attack, `Prime+Probe` [102,124], in *userspace-only scenarios*. To do so, we conduct an end-to-end experiment, by leveraging Mastik [119], a micro-architectural side channel toolkit, to perform `Prime+Probe` and log victim's access toward L1D and L1I cache. We use Linux `taskset` to pin the victim software and the `spy` process on the same CPU core. We launch experiments on both Intel Xeon CPU and AMD Ryzen CPU. See Appx. D for setup details of this end-to-end attack. We also clarify how cache side channels are represented and processed by our encoder in Appx. F.

The quantitative evaluation results, as reported in Table 12, are generally encouraging. Attacks toward `libjpeg` and `Hunspell` manifest high accuracy comparable with attacks over `Pin`-logged traces (Sec. 6.1.2). While `Prime+Probe` logs relatively noisier cache side channels, our attack shows promising noise resilience, as trace encoder (and manifold learning by design) is noise resilient. Further, the logged

Table 12: Quantitative evaluation results using cache side channels logged by `Prime+Probe`. We also provide the processing time (*ms*) when launching `Prime+Probe` (normal → with `Prime+Probe`).

	`FFmpeg` & SC09 voice matching		`libjpeg` & CelebA face matching/non-face		`Hunspell` & DDialog text matching	
	Intel	**AMD**	**Intel**	**AMD**	**Intel**	**AMD**
L1I Cache	12.6% (36 → 580)	11.6% (10 → 420)	38.0/0.85% (5 → 18)	35.9/1.2% (2 → 22)	33.9% (60 → 130)	33.2% (23 → 60)
L1D Cache	81.8% (36 → 590)	15.7% (10 → 420)	36.9/0.80% (5 → 20)	33.9/0.90% (2 → 24)	32.2% (60 → 130)	31.8% (23 → 60)

side channels are *sparse*; given only a few records are secret-dependent, noise introduced by `Prime+Probe` and other workloads do not primarily impede our attack. See further discussion on noise resilience in Appx. F.

`FFmpeg` reports high attack accuracy (over 80%) on Intel L1D cache but lower accuracy for other settings. As will be reported in Table 15 (Appx. D), the logged side channel traces are unstable (and challenging to comprehend), where stddev is about half of the average trace length. To verify the high attack accuracy on Intel L1D cache, we manually checked all the reconstructed 2,552 audio clips (also uploaded at [3] for the reference). The reconstructed audio clips on Intel L1D cache manifest high quality. However, while the original audio clips of the same class are produced by different persons (and sound very different), all reconstructed audio clips of the same class sound *indistinguishable*. This indicates that the trained model stealthily simplifies the task of reconstruction into a task of ten class-conditional generation (recall this dataset has "0–9" labels). We then manually checked the collected traces: we find that for this particular case, Intel L1D cache "amplifies" the distance of inter-class traces while reduces the distance of intra-class traces. As a result, intra-class differences are not well learned using training data. However, since our quantitative metrics only check if the reconstructed audio can be classified correctly, the attack accuracy is high, indicating privacy leakage. We use attention (Sec. 4.2) and compared all the localized code components contributing side channels: we report that localized functions are the *same* on Intel/AMD CPUs. However, they manifest different frequencies, which result in this subtle model decaying. We confirm that this stealthy issue *only* occurs for this case. To solve this issue (and therefore reconstruct diverse outputs within the same class), users can opt for more complex models or larger training data, if needed.

Overall, inspired by recent work [112] exploring timing-based microarchitectural side channels, we deem it an interesting future work to benchmark the microarchitectural side channel differences. Our tool can automatically check whether side channels are informative enough to reconstruct secrets, when it largely outperforms the baseline.

We report the slowdown incurred by `Prime+Probe` attack in Table 12. Overall, media software are highly complex, and processing media data can usually induce a large volume of cache accesses. This way, frequent cache misses due to `Prime+Probe` can cause a reasonably high slowdown. Appx. D gives further discussion regarding this point. We also present qualitative evaluation results in Appx. D. In short, the reconstructed media data (e.g., images) manifest fairly high visual quality. For instance, the reconstructed CelebA face photos retain many correct perception features, such as face orientation, skin color, hair color and hair styles.

Table 13: Attack PathOHeap.

Function	`IDCT`	`MCU`
w/o ORAM	40.3%	38.0%
with ORAM	0.2%	0.2%

6.5 Mitigation Using ORAM

Besides perception blinding, this section assesses other mitigations. Existing mitigations aim at adding randomness, making it constant, or directly masking inputs. Nearly all of them are particularly designed to protect crypto software [21, 31, 101]. Raccoon [87] proposes general mitigation using software obfuscation; however, its implementation is not available. That said, oblivious RAM (ORAM) [42] conceal memory access sequences of a program by continuously shuffling data as they are accessed. We study whether a representative ORAM, PathOHeap [97], can mitigate our attack. Due to the limited space, we report the key evaluation results in Table 13. PathOHeap takes several hours to process one memory access made by `libjpeg`. We thus focus on two critical functions localized by our framework (see Sec. 6.2), `IDCT` and `MCU`, separately.[6] We measure attack success rates with and w/o first converting memory traces using PathOHeap.

Cache line side channels derived from either `IDCT` or `MCU` are sufficient for attack. Nevertheless, ORAM eliminates information leak: memory access traces, after processed by PathOHeap, do *not* depend on input images. We report that our autoencoder does not even reach convergence during training, and the reconstructed images (using poorly trained autoencoder) show indistinguishable and meaningless visual appearances. The non-zero result (i.e., 0.2%) is because that many face photos look like an "average" face. In other words, 0.2% implies the *baseline* of face matching.

Comparison. PathOHeap is very costly: while `libjpeg` can process an image within 100ms, PathOHeap takes several hours to convert the corresponding memory trace. The obfuscator, Racoon [87], has an average overhead of 16.1×. In

[6] Focusing on functions with known information leakage (i.e., `IDCT`) [45, 117] demonstrates a "white-box" attacker using our technique.

Table 14: Quantitative evaluation results (same face/non-face) of face images reconstructed from noisy side channels.

Setting	Noise Insertion Scheme	NA	Low	High
`Pin` logged trace	**Gaussian**	43.5/2.0%	33.8/2.1%	28.0/1.5%
	Shifting	43.5/2.0%	42.9/1.7%	39.1/1.8%
	Removal	43.5/2.0%	30.0/1.9%	29.3/4.3%
`Prime+Probe` logged trace	**Leave out**	36.9/0.8%	36.8/1.1%	36.8/1.1%
	False hit/miss	36.9/0.8%	36.4/1.2%	36.1/1.2%
	Wrong order	36.9/0.8%	36.8/1.0%	36.7/1.0%
Workload under `Prime+Probe`	**Bzip2**	36.9/0.8%	27.6/1.0%	
	Victim$_1$	36.9/0.8%	30.7/1.1%	
	Victim$_2$	36.9/0.8%	29.0/1.0%	

contrast, perception-blinding delivers negligible extra cost (i.e., processing masked data using media software once) albeit its mitigation is specific for manifold learning-based SCA. This underlines the key novelty of our technique.

6.6 Noise Resilience

We have discussed the general immunity to noise of manifold learning in Fig. 3. This section empirically assesses our attacks under various scenarios where noise is introduced in side channels. We summarize our noise insertion schemes in Table 14. The first three schemes are launched to mutate cache line access traces logged by `Pin`, whereas the latter three mutate the cache set hit/miss records logged via `Prime+Probe`. **NA** means no noise is inserted, whereas **Low/High** denote to what extent side channel logs are perturbed (see Appx. I for details). We also benchmark how real-world workload, i.e., by launching `bzip2` or another victim software (e.g., `libjpeg`) on the same CPU core, can undermine our attack. **Victim$_1$** and **Victim$_2$** represent launching another victim software on the same core and processing the same or different inputs.

Due to the limited space, we only report the quantitative evaluation results of `libjpeg` on CelebA in Table 14. See Appx. I for other quantitative and qualitative results: despite the applied noise, many perceptual features are still retained in the reconstructed data (e.g., face photos), illustrating capability of privacy stealing under noisy scenarios.

The reconstructed images are more resilient toward **Shifting**. **Removal** and **Gaussian** noise, by extensively leaving out or perturbing data points on the logged trace (e.g., **Removal/High** removes *half* records on a trace), show greater influence on data reconstruction. As for noise inserted in `Prime+Probe` logged side channel records, none of them primarily affect the attack accuracy. We note that `Prime+Probe` logged side channel traces, even without applying these noise insertion schemes, are of high stddev. That is, our autoencoder will be trained with more "diverse" side channel logs, which enhance the robustness but undermines accuracy. Similar findings are obtained in launching extra real-world workloads. Please refer to Appx. I for further evaluation on noise resilience, and our analysis on noise resilience from the trace encoder structure perspective and training data perspective.

7 Related Work

Side Channel Analysis. Kocher proposes to use timing side channel to exploit crypto systems [55]. To date, side channels have been used to exploit crypto systems under different scenarios [9, 13, 35, 116], including trusted computing environments like Intel SGX [16, 64, 79, 93]. [22] demonstrates that timing side channel can be launched remotely through network. The CPU cache are particularly exploited given its indispensable role in boosting modern computing platforms [45, 74, 83, 121]. Controlled side channel assumes an adversarial-controlled OS to log page table access of victim software [117]. DNNs have been used to infer secret keys from crypto libraries [48, 49, 77]. These works, usually referred to as "profiled SCA", share the same assumption with our research that models are trained using historical data. Most existing DNN-based SCA focuses on attacking crypto systems; they typically perform low-level *bit-wise classification* to gradually infer key bits. In contrast, we show that attackers in black-box scenarios can use manifold learning to reconstruct media data of various types in an end-to-end manner. [61, 115] also use autoencoders in the context of SCA. However, they use autoencoder to denoise side channel traces as a *preprocessing* step for SCA of crypto software.

Countermeasures. Software-based techniques include constant-time techniques which ensure that software behavior is independent with its confidential data [30, 56, 80, 86, 92]. Techniques have also been proposed to blind secrets or randomize side channel access patterns [11, 17, 33, 52, 58, 87]. ORAM [43, 72, 97, 98] translates memory access into identical or indistinguishable traces, which can provably eliminate many side channels but incur high performance penalty. Program analysis methods such as information flow tracking [62, 81], model checking [10], type system [8, 89], abstract interpretation [36, 57, 104], and constraint solving [19, 105] are used to check crypto software and detect side channels. In contrast, our study delivers a *neural attention*-based approach to detecting code fragments inducing information leakage. Hardware-based countermeasures include randomizing side channel access or enforcing fine-grained resource isolation [73, 84, 107–109]. Compared with system- and hardware-based countermeasures, software-based approaches usually do not require to modify the underlying hardware design. Nevertheless, software-based countermeasures are generally high cost and low scalable in analyzing real-world software.

8 Conclusion

This research proposes SCA for media software. We perform cross-modality manifold learning to reconstruct media data from side channel traces. We also use attention to localize program points leading information leakage. We design perception blinding to mitigate the proposed SCA. Our evaluation on real-world media software reports promising results.

References

[1] FFMPEG. https://ffmpeg.org/.

[2] hunspell. http://hunspell.github.io/.

[3] Research artifact. https://github.com/Yuanyuan-Yuan/Manifold-SCA.

[4] Chest x-ray competition. https://stanfordmlgroup.github.io/competitions/chexpert/, 2020.

[5] Face attributes analysis service. https://www.faceplusplus.com/attributes/, 2020.

[6] PAGE MASK. https://elixir.bootlin.com/linux/v5.6.10/source/arch/x86/include/asm/page_types.h, 2020.

[7] Hervé Abdi and Lynne J Williams. Principal component analysis. *Wiley interdisciplinary reviews: computational statistics*, 2(4):433–459, 2010.

[8] Johan Agat. Transforming out timing leaks. In *Proceedings of the 27th ACM SIGPLAN-SIGACT symposium on Principles of programming languages*, pages 40–53, 2000.

[9] Nadhem J Al Fardan and Kenneth G Paterson. Lucky thirteen: Breaking the tls and dtls record protocols. In *2013 IEEE Symposium on Security and Privacy*, pages 526–540. IEEE, 2013.

[10] José Bacelar Almeida, Manuel Barbosa, Gilles Barthe, François Dupressoir, and Michael Emmi. Verifying constant-time implementations. In *USENIX Sec.*, 2016.

[11] Aslan Askarov, Danfeng Zhang, and Andrew C Myers. Predictive black-box mitigation of timing channels. In *Proceedings of the 17th ACM conference on Computer and communications security*, pages 297–307, 2010.

[12] Mukund Balasubramanian, Eric L Schwartz, Joshua B Tenenbaum, Vin de Silva, and John C Langford. The ISOMAP algorithm and topological stability. *Science*, 295(5552):7–7, 2002.

[13] Lucas Bang, Abdulbaki Aydin, Quoc-Sang Phan, Corina S Păsăreanu, and Tevfik Bultan. String analysis for side channels with segmented oracles. In *Proceedings of the 2016 24th ACM SIGSOFT International Symposium on Foundations of Software Engineering*, pages 193–204, 2016.

[14] Mikhail Belkin and Partha Niyogi. Laplacian eigenmaps and spectral techniques for embedding and clustering. In *Nips*, volume 14, pages 585–591, 2001.

[15] Yoshua Bengio, Aaron Courville, and Pascal Vincent. Representation learning: A review and new perspectives. *IEEE transactions on pattern analysis and machine intelligence*, 35(8):1798–1828, 2013.

[16] Ferdinand Brasser, Urs Müller, Alexandra Dmitrienko, Kari Kostiainen, Srdjan Capkun, and Ahmad-Reza Sadeghi. Software grand exposure: SGX cache attacks are practical. In *Proceedings of the 11th USENIX Workshop on Offensive Technologies (WOOT' 17)*, 2017.

[17] Benjamin A Braun, Suman Jana, and Dan Boneh. Robust and efficient elimination of cache and timing side channels. *arXiv preprint arXiv:1506.00189*, 2015.

[18] Andrew Brock, Jeff Donahue, and Karen Simonyan. Large scale GAN training for high fidelity natural image synthesis. In *International Conference on Learning Representations*, 2019.

[19] Robert Brotzman, Shen Liu, Danfeng Zhang, Gang Tan, and Mahmut Kandemir. CaSym: Cache aware symbolic execution for side channel detection and mitigation. In *IEEE SP*, 2018.

[20] Robert Brotzman, Shen Liu, Danfeng Zhang, Gang Tan, and Mahmut Kandemir. CaSym: Cache aware symbolic execution for side channel detection and mitigation. In *2019 IEEE Symposium on Security and Privacy (SP)*, pages 505–521. IEEE, 2019.

[21] David Brumley and Dan Boneh. Remote timing attacks are practical. *Computer Networks*, 48(5):701–716, 2005.

[22] David Brumley and Dan Boneh. Remote timing attacks are practical. *Computer Networks*, January 2005.

[23] Eleonora Cagli, Cécile Dumas, and Emmanuel Prouff. Convolutional neural networks with data augmentation against jitter-based countermeasures. In *International Conference on Cryptographic Hardware and Embedded Systems*, pages 45–68. Springer, 2017.

[24] Nicholas Carlini, Chang Liu, Úlfar Erlingsson, Jernej Kos, and Dawn Song. The secret sharer: Evaluating and testing unintended memorization in neural networks. In *28th {USENIX} Security Symposium ({USENIX} Security 19)*, pages 267–284, 2019.

[25] Ya Chang, Changbo Hu, and Matthew Turk. Manifold of facial expression. In *AMFG*, pages 28–35, 2003.

[26] Ya-Liang Chang, Kuan-Ying Lee, Po-Yu Wu, Hung-yi Lee, and Winston Hsu. Deep long audio inpainting. *arXiv preprint arXiv:1911.06476*, 2019.

[27] Lele Chen, Sudhanshu Srivastava, Zhiyao Duan, and Chenliang Xu. Deep cross-modal audio-visual generation. In *Proceedings of the on Thematic Workshops of ACM Multimedia 2017*, pages 349–357, 2017.

[28] Mikhail Chernov and Eric Ghysels. A study towards a unified approach to the joint estimation of objective and risk neutral measures for the purpose of options valuation. *Journal of financial economics*, 56(3):407–458, 2000.

[29] R. C. Chiang, S. Rajasekaran, N. Zhang, and H. H. Huang. Swiper: Exploiting virtual machine vulnerability in third-party clouds with competition for i/o resources. *IEEE Transactions on Parallel and Distributed Systems*, 26(6):1732–1742, June 2015.

[30] Bart Coppens, Ingrid Verbauwhede, Koen De Bosschere, and Bjorn De Sutter. Practical mitigations for timing-based side-channel attacks on modern x86 processors. In *IEEE SP*, 2009.

[31] Jean-Sébastien Coron and Ilya Kizhvatov. An efficient method for random delay generation in embedded software. In *International Workshop on Cryptographic Hardware and Embedded Systems*, pages 156–170. Springer, 2009.

[32] Jose A Costa and Alfred O Hero. Geodesic entropic graphs for dimension and entropy estimation in manifold learning. *IEEE Transactions on Signal Processing*, 52(8):2210–2221, 2004.

[33] Stephen Crane, Andrei Homescu, Stefan Brunthaler, Per Larsen, and Michael Franz. Thwarting cache side-channel attacks through dynamic software diversity. NDSS, 2015.

[34] Craig Disselkoen, David Kohlbrenner, Leo Porter, and Dean Tullsen. Prime+Abort: A timer-free high-precision L3 cache attack using Intel TSX. In *USENIX Sec.*, 2017.

[35] Xiaowan Dong, Zhuojia Shen, John Criswell, Alan L Cox, and Sandhya Dwarkadas. Shielding software from privileged side-channel attacks. In *27th USENIX Security Symposium*, pages 1441–1458, 2018.

[36] Goran Doychev, Dominik Feld, Boris Kopf, Laurent Mauborgne, and Jan Reineke. CacheAudit: A tool for the static analysis of cache side channels. In *USENIX Sec.*, 2013.

[37] Goran Doychev and Boris Köpf. Rigorous analysis of software countermeasures against cache attacks. In *Proceedings of the 38th ACM Conference on Programming Language Design and Implementation (PLDI)*, 2017.

[38] Bin Duan, Wei Wang, Hao Tang, Hugo Latapie, and Yan Yan. Cascade attention guided residue learning gan for cross-modal translation. *arXiv preprint arXiv:1907.01826*, 2019.

[39] Xing Fan, Wei Jiang, Hao Luo, and Mengjuan Fei. Spherereid: Deep hypersphere manifold embedding for person re-identification. *Journal of Visual Communication and Image Representation*, 60:51–58, 2019.

[40] Charles Fefferman, Sanjoy Mitter, and Hariharan Narayanan. Testing the manifold hypothesis. *Journal of the American Mathematical Society*, 29(4):983–1049, 2016.

[41] Zhenyong Fu, Tao Xiang, Elyor Kodirov, and Shaogang Gong. Zero-shot object recognition by semantic manifold distance. In *Proceedings of the IEEE conference on computer vision and pattern recognition*, pages 2635–2644, 2015.

[42] Oded Goldreich. Towards a theory of software protection and simulation by oblivious rams. In *Proceedings of the nineteenth annual ACM symposium on Theory of computing*, pages 182–194, 1987.

[43] Oded Goldreich and Rafail Ostrovsky. Software protection and simulation on oblivious rams. *Journal of the ACM (JACM)*, 43(3):431–473, 1996.

[44] Ian Goodfellow, Jean Pouget-Abadie, Mehdi Mirza, Bing Xu, David Warde-Farley, Sherjil Ozair, Aaron Courville, and Yoshua Bengio. Generative adversarial nets. In *Advances in neural information processing systems*, pages 2672–2680, 2014.

[45] Marcus Hähnel, Weidong Cui, and Marcus Peinado. High-resolution side channels for untrusted operating systems. In *2017 USENIX Annual Technical Conference*, pages 299–312, 2017.

[46] Xiaofei He, Shuicheng Yan, Yuxiao Hu, Partha Niyogi, and Hong-Jiang Zhang. Face recognition using laplacianfaces. *IEEE transactions on pattern analysis and machine intelligence*, 27(3):328–340, 2005.

[47] Benjamin Hettwer, Stefan Gehrer, and Tim Güneysu. Profiled power analysis attacks using convolutional neural networks with domain knowledge. In *International Conference on Selected Areas in Cryptography*, pages 479–498. Springer, 2018.

[48] Benjamin Hettwer, Tobias Horn, Stefan Gehrer, and Tim Güneysu. Encoding power traces as images for efficient side-channel analysis. *arXiv preprint arXiv:2004.11015*, 2020.

[49] Annelie Heuser and Michael Zohner. Intelligent machine homicide. In *International Workshop on Constructive Side-Channel Analysis and Secure Design*, pages 249–264. Springer, 2012.

[50] Geoffrey E Hinton and Richard S Zemel. Autoencoders, minimum description length, and helmholtz free energy. *Advances in neural information processing systems*, 6:3–10, 1994.

[51] Daniel Holden, Jun Saito, Taku Komura, and Thomas Joyce. Learning motion manifolds with convolutional autoencoders. In *SIGGRAPH Asia 2015 Technical Briefs*, pages 1–4. 2015.

[52] Wei-Ming Hu. Reducing timing channels with fuzzy time. *Journal of computer security*, 1(3-4):233–254, 1992.

[53] Gorka Irazoqui, Kai Cong, Xiaofei Guo, Hareesh Khattri, Arun K. Kanuparthi, Thomas Eisenbarth, and Berk Sunar. Did we learn from LLC side channel attacks? A cache leakage detection tool for crypto libraries. *CoRR*, 2017.

[54] Jaehun Kim, Stjepan Picek, Annelie Heuser, Shivam Bhasin, and Alan Hanjalic. Make some noise. unleashing the power of convolutional neural networks

for profiled side-channel analysis. *IACR Transactions on Cryptographic Hardware and Embedded Systems*, pages 148–179, 2019.

[55] Paul C. Kocher. Timing attacks on implementations of Diffie-Hellman, RSA, DSS, and other systems. In *Proceedings of the 16th Annual International Cryptology Conference on Advances in Cryptology*, CRYPTO '96. Springer-Verlag, 1996.

[56] Boris Köpf and Heiko Mantel. Transformational typing and unification for automatically correcting insecure programs. *International Journal of Information Security*, 6(2-3):107–131, 2007.

[57] Boris Köpf, Laurent Mauborgne, and Martín Ochoa. Automatic quantification of cache side-channels. In *International Conference on Computer Aided Verification*, pages 564–580. Springer, 2012.

[58] Boris Köpf and Geoffrey Smith. Vulnerability bounds and leakage resilience of blinded cryptography under timing attacks. In *2010 23rd IEEE Computer Security Foundations Symposium*, pages 44–56. IEEE, 2010.

[59] Alex Krizhevsky, Geoffrey Hinton, et al. Learning multiple layers of features from tiny images. 2009.

[60] Solomon Kullback and Richard A Leibler. On information and sufficiency. *The annals of mathematical statistics*, 22(1):79–86, 1951.

[61] Donggeun Kwon, HeeSeok Kim, and Seokhie Hong. Improving non-profiled side-channel attacks using autoencoder based preprocessing. *IACR Cryptol. ePrint Arch.*, 2020:396, 2020.

[62] Adam Langley. ctgrind. https://github.com/agl/ctgrind.

[63] Yann LeCun, Fu Jie Huang, and Leon Bottou. Learning methods for generic object recognition with invariance to pose and lighting. In *Proceedings of the 2004 IEEE Computer Society Conference on Computer Vision and Pattern Recognition, 2004. CVPR 2004.*, volume 2, pages II–104. IEEE, 2004.

[64] Dayeol Lee, Dongha Jung, Ian T Fang, Chia-Che Tsai, and Raluca Ada Popa. An off-chip attack on hardware enclaves via the memory bus. In *29th {USENIX} Security Symposium ({USENIX} Security 20)*, 2020.

[65] John A Lee and Michel Verleysen. *Nonlinear dimensionality reduction*. Springer Science & Business Media, 2007.

[66] Bochen Li, Xinzhao Liu, Karthik Dinesh, Zhiyao Duan, and Gaurav Sharma. Creating a multitrack classical music performance dataset for multimodal music analysis: Challenges, insights, and applications. *IEEE Transactions on Multimedia*, 21(2):522–535, 2018.

[67] Haoqi Li, Brian Baucom, and Panayiotis Georgiou. Unsupervised latent behavior manifold learning from acoustic features: Audio2behavior. In *2017 IEEE international conference on acoustics, speech and signal processing (ICASSP)*, pages 5620–5624. IEEE, 2017.

[68] Yanran Li, Hui Su, Xiaoyu Shen, Wenjie Li, Ziqiang Cao, and Shuzi Niu. Dailydialog: A manually labelled multi-turn dialogue dataset. *arXiv preprint arXiv:1710.03957*, 2017.

[69] libjpeg. Main libjpeg-turbo repository, 2020.

[70] Tong Lin and Hongbin Zha. Riemannian manifold learning. *IEEE Transactions on Pattern Analysis and Machine Intelligence*, 30(5):796–809, 2008.

[71] Tsung-Yi Lin, Michael Maire, Serge Belongie, James Hays, Pietro Perona, Deva Ramanan, Piotr Dollár, and C Lawrence Zitnick. Microsoft COCO: Common objects in context. In *European conference on computer vision*, pages 740–755. Springer, 2014.

[72] Chang Liu, Austin Harris, Martin Maas, Michael Hicks, Mohit Tiwari, and Elaine Shi. Ghostrider: A hardware-software system for memory trace oblivious computation. *ACM SIGPLAN Notices*, 50(4):87–101, 2015.

[73] F. Liu, Q. Ge, Y. Yarom, F. Mckeen, C. Rozas, G. Heiser, and R. B. Lee. Catalyst: Defeating last-level cache side channel attacks in cloud computing. In *HPCA*, 2016.

[74] Fangfei Liu, Y. Yarom, Qian Ge, G. Heiser, and R.B. Lee. Last-level cache side-channel attacks are practical. In *2015 IEEE Symposium on Security and Privacy*, pages 605–622, May 2015.

[75] Ziwei Liu, Ping Luo, Xiaogang Wang, and Xiaoou Tang. Deep learning face attributes in the wild. In *Proceedings of International Conference on Computer Vision (ICCV)*, December 2015.

[76] Chi-Keung Luk, Robert Cohn, Robert Muth, Harish Patil, Artur Klauser, Geoff Lowney, Steven Wallace, Vijay Janapa Reddi, and Kim Hazelwood. Pin: building customized program analysis tools with dynamic instrumentation. In *Proceedings of the 2005 ACM SIGPLAN conference on Programming language design and implementation (PLDI'05)*, 2005.

[77] Houssem Maghrebi, Thibault Portigliatti, and Emmanuel Prouff. Breaking cryptographic implementations using deep learning techniques. In *International Conference on Security, Privacy, and Applied Cryptography Engineering*, pages 3–26. Springer, 2016.

[78] Francisco J Martinez-Murcia, Andres Ortiz, Juan-Manuel Gorriz, Javier Ramirez, and Diego Castillo-Barnes. Studying the manifold structure of alzheimer's disease: A deep learning approach using convolutional autoencoders. *IEEE journal of biomedical and health informatics*, 24(1):17–26, 2019.

[79] Ahmad Moghimi, Gorka Irazoqui, and Thomas Eisenbarth. CacheZoom: How sgx amplifies the power of cache attacks. In *International Conference on Cryptographic Hardware and Embedded Systems (CHES' 17)*, 2017.

[80] David Molnar, Matt Piotrowski, David Schultz, and David Wagner. The program counter security model:

Automatic detection and removal of control-flow side channel attacks. In *ICISC*, 2005.

[81] Andrew C Myers. JFlow: Practical mostly-static information flow control. In *Proceedings of the 26th ACM SIGPLAN-SIGACT symposium on Principles of programming languages*, pages 228–241, 1999.

[82] Openssl. https://www.openssl.org/.

[83] Yossef Oren, Vasileios P Kemerlis, Simha Sethumadhavan, and Angelos D Keromytis. The spy in the sandbox: Practical cache attacks in javascript and their implications. In *Proceedings of the 22nd ACM SIGSAC Conference on Computer and Communications Security*, pages 1406–1418, 2015.

[84] D Page. Partitioned cache architecture as a ėide-channel defence mechanism. 2005.

[85] Stjepan Picek, Ioannis Petros Samiotis, Jaehun Kim, Annelie Heuser, Shivam Bhasin, and Axel Legay. On the performance of convolutional neural networks for side-channel analysis. In *International Conference on Security, Privacy, and Applied Cryptography Engineering*, pages 157–176. Springer, 2018.

[86] Himanshu Raj, Ripal Nathuji, Abhishek Singh, and Paul England. Resource management for isolation enhanced cloud services. In *CCSW*, 2009.

[87] Ashay Rane, Calvin Lin, and Mohit Tiwari. Raccoon: Closing digital side-channels through obfuscated execution. In *24th {USENIX} Security Symposium ({USENIX} Security 15)*, pages 431–446, 2015.

[88] Sam T Roweis and Lawrence K Saul. Nonlinear dimensionality reduction by locally linear embedding. *science*, 290(5500):2323–2326, 2000.

[89] Andrei Sabelfeld and Andrew C Myers. Language-based information-flow security. *IEEE Journal on selected areas in communications*, 21(1):5–19, 2003.

[90] Yuki Saito, Shinnosuke Takamichi, and Hiroshi Saruwatari. Statistical parametric speech synthesis incorporating generative adversarial networks. *IEEE/ACM Transactions on Audio, Speech, and Language Processing*, 26(1):84–96, 2017.

[91] Florian Schroff, Dmitry Kalenichenko, and James Philbin. Facenet: A unified embedding for face recognition and clustering. In *Proceedings of the IEEE conference on computer vision and pattern recognition*, pages 815–823, 2015.

[92] Michael Schwarz, Moritz Lipp, Daniel Gruss, Samuel Weiser, Clémentine Maurice, Raphael Spreitzer, and Stefan Mangard. KeyDrown: Eliminating software-based keystroke timing side-channel attacks. In *NDSS*, 2018.

[93] Michael Schwarz, Samuel Weiser, Daniel Gruss, Clémentine Maurice, and Stefan Mangard. Malware guard extension: Using sgx to conceal cache attacks. *arXiv preprint arXiv:1702.08719*, 2017.

[94] Dongdong She, Yizheng Chen, Abhishek Shah, Baishakhi Ray, and Suman Jana. Neutaint: Efficient dynamic taint analysis with neural networks. In *2020 IEEE Symposium on Security and Privacy (SP)*, pages 1527–1543. IEEE, 2020.

[95] Dongdong She, Kexin Pei, Dave Epstein, Junfeng Yang, Baishakhi Ray, and Suman Jana. NEUZZ: Efficient fuzzing with neural program smoothing. In *Proceedings of the 40th IEEE Symposium on Security and Privacy (S&P '19)*, 2019.

[96] Yujun Shen, Jinjin Gu, Xiaoou Tang, and Bolei Zhou. Interpreting the latent space of gans for semantic face editing. In *Proceedings of the IEEE/CVF Conference on Computer Vision and Pattern Recognition*, pages 9243–9252, 2020.

[97] Elaine Shi. Path oblivious heap: Optimal and practical oblivious priority queue. In *2020 IEEE Symposium on Security and Privacy (SP)*, pages 842–858. IEEE, 2020.

[98] Emil Stefanov, Marten Van Dijk, Elaine Shi, Christopher Fletcher, Ling Ren, Xiangyao Yu, and Srinivas Devadas. Path ORAM: an extremely simple oblivious ram protocol. In *Proceedings of the 2013 ACM SIGSAC conference on Computer & communications security*, pages 299–310, 2013.

[99] Joshua B Tenenbaum, Vin De Silva, and John C Langford. A global geometric framework for nonlinear dimensionality reduction. *science*, 290(5500):2319–2323, 2000.

[100] Nicolas Thorstensen. *Manifold learning and applications to shape and image processing*. PhD thesis, Ecole des Ponts ParisTech, 2009.

[101] Kris Tiri and Ingrid Verbauwhede. Securing encryption algorithms against dpa at the logic level: Next generation smart card technology. In *International Workshop on Cryptographic Hardware and Embedded Systems*, pages 125–136. Springer, 2003.

[102] Eran Tromer, DagArne Osvik, and Adi Shamir. Efficient cache attacks on AES, and countermeasures. *Journal of Cryptology*, 23(1):37–71, 2010.

[103] Ashish Vaswani, Noam Shazeer, Niki Parmar, Jakob Uszkoreit, Llion Jones, Aidan N Gomez, Lukasz Kaiser, and Illia Polosukhin. Attention is all you need. *arXiv preprint arXiv:1706.03762*, 2017.

[104] Shuai Wang, Yuyan Bao, Xiao Liu, Pei Wang, Danfeng Zhang, and Dinghao Wu. Identifying cache-based side channels through secret-augmented abstract interpretation. In *28th {USENIX} Security Symposium ({USENIX} Security 19)*, pages 657–674, 2019.

[105] Shuai Wang, Pei Wang, Xiao Liu, Danfeng Zhang, and Dinghao Wu. CacheD: Identifying cache-based timing channels in production software. In *26th USENIX Security Symposium*, pages 235–252, 2017.

[106] Xiaosong Wang, Yifan Peng, Le Lu, Zhiyong Lu, Mohammadhadi Bagheri, and Ronald M Summers. Chestx-ray8: Hospital-scale chest x-ray database and benchmarks on weakly-supervised classification and localization of common thorax diseases. In *Proceedings of the IEEE conference on computer vision and pattern recognition*, pages 2097–2106, 2017.

[107] Zhenghong Wang and Ruby B. Lee. Covert and side channels due to processor architecture. In *ACSAC*, 2006.

[108] Zhenghong Wang and Ruby B. Lee. New cache designs for thwarting software cache-based side channel attacks. In *ISCA*, 2007.

[109] Zhenghong Wang and Ruby B Lee. A novel cache architecture with enhanced performance and security. In *MICRO*, 2008.

[110] Zhou Wang, Alan C Bovik, Hamid R Sheikh, and Eero P Simoncelli. Image quality assessment: from error visibility to structural similarity. *IEEE transactions on image processing*, 13(4):600–612, 2004.

[111] Pete Warden. Speech commands: A dataset for limited-vocabulary speech recognition. *arXiv preprint arXiv:1804.03209*, 2018.

[112] Daniel Weber, Ahmad Ibrahim, Hamed Nemati, Michael Schwarz, and Christian Rossow. Osiris: Automatic Discovery of Microarchitectural Side Channels. In *USENIX Security Symposium*, 2021.

[113] Jan Wichelmann, Ahmad Moghimi, Thomas Eisenbarth, and Berk Sunar. MicroWalk: A framework for finding side channels in binaries. In *ACSAC*, 2018.

[114] Sanghyun Woo, Jongchan Park, Joon-Young Lee, and In So Kweon. Cbam: Convolutional block attention module. In *Proceedings of the European conference on computer vision (ECCV)*, pages 3–19, 2018.

[115] Lichao Wu and Stjepan Picek. Remove some noise: On pre-processing of side-channel measurements with autoencoders. *IACR Transactions on Cryptographic Hardware and Embedded Systems*, pages 389–415, 2020.

[116] Zhenyu Wu, Zhang Xu, and Haining Wang. Whispers in the hyper-space: High-speed covert channel attacks in the cloud. In *Presented as part of the 21st USENIX Security Symposium (USENIX Security 12)*, pages 159–173, 2012.

[117] Yuanzhong Xu, Weidong Cui, and Marcus Peinado. Controlled-channel attacks: Deterministic side channels for untrusted operating systems. In *2015 IEEE Symposium on Security and Privacy*, pages 640–656. IEEE, 2015.

[118] Guang Yang, Huizhong Li, Jingdian Ming, and Yongbin Zhou. Convolutional neural network based side-channel attacks in time-frequency representations. In *International Conference on Smart Card Research and Advanced Applications*, pages 1–17. Springer, 2018.

[119] Yuval Yarom. Mastik: A micro-architectural side-channel toolkit. *Retrieved from School of Computer Science Adelaide: http://cs.adelaide.edu.au/yval/Mastik*, 16, 2016.

[120] Yuval Yarom and Katrina Falkner. FLUSH+RELOAD: A high resolution, low noise, L3 cache side-channel attack. In *Proceedings of the 23rd USENIX Conference on Security Symposium*, pages 719–732, 2014.

[121] Yuval Yarom, Daniel Genkin, and Nadia Heninger. Cachebleed: a timing attack on openssl constant-time rsa. *Journal of Cryptographic Engineering*, 7(2):99–112, 2017.

[122] Yuanyuan Yuan, Qi Pang, and Shuai Wang. Automated side channel analysis of media software with manifold learning. In *31st USENIX Security Symposium (USENIX Security 22)*, Boston, MA, August 2022. USENIX Association.

[123] Yuanyuan Yuan, Shuai Wang, and Junping Zhang. Private image reconstruction from system side channels using generative models. In *International Conference on Learning Representations*, 2021.

[124] Yinqian Zhang, Ari Juels, Michael K. Reiter, and Thomas Ristenpart. Cross-VM side channels and their use to extract private keys. In *Proceedings of the 2012 ACM Conference on Computer and Communications Security*, pages 305–316, 2012.

[125] Bo Zhu, Jeremiah Z Liu, Stephen F Cauley, Bruce R Rosen, and Matthew S Rosen. Image reconstruction by domain-transform manifold learning. *Nature*, 555(7697):487–492, 2018.

[126] Jun-Yan Zhu, Philipp Krähenbühl, Eli Shechtman, and Alexei A Efros. Generative visual manipulation on the natural image manifold. In *European conference on computer vision*, pages 597–613. Springer, 2016.

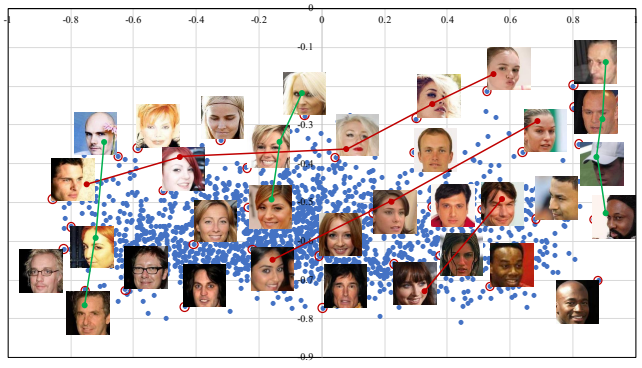


Figure 8: Project face photos to a two-dimensional manifold.

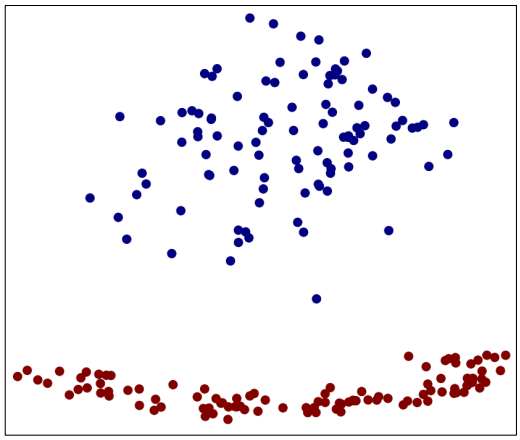


Figure 9: Applying PCA on two classes of images from MNIST dataset.

A Empirical Exploration of Manifold Hypothesis

This section empirically explores the validity of the manifold hypothesis. In Fig. 8, a set of real-world face images is projected onto manifold $\mathcal{M}_{img}$ of two dimensions. To draw this projection, we adjust our autoencoder framework (see Sec. 4) to convert each face image into a latent representation of two dimensions. We observe that the images are generally distinguished by skin and hair colors, and face orientations are roughly decomposed into two orthogonal directions (green and red lines). For instance, the photos at the bottom right and bottom left are grouped together with similar hair colors but are further differentiated due to differences in skin colors and face directions. Overall, we interpret that Fig. 8 provides clear evidence that our autoencoder frameworks can capture key perception features of complex high-dimensional media data. In addition, because 2D projections are highly condensed for real-world large datasets, we expect to find greater discrimination for higher dimensions (e.g., 64).

In fact, recent studies have shown the effectiveness of conducting image editing by first projecting image samples into the manifold space [96, 126]. Editing images in the high-dimensional space involves a large search space $[0,255]$ for each pixel; the random selection of pixel values in the range $[0,255]$ struggles to create realistic images because arbitrary editing could "fall off" the manifold of natural images. In contrast, manifold learning facilitates sampling within $\mathcal{M}$, and the perceptually meaningful contents in $\mathcal{M}$ confine the manipulations to generate mostly realistic images [96, 126].

Furthermore, as introduced in Sec. 3, the manifold learning hypothesis also assumes that after casting high-dimensional data into their low-dimensional space (i.e., manifolds), data of different classes can be well separated whereas data of the same class generally lies in the same manifold [100]. Accordingly, our preliminary study confirmed this hypothesis: as shown in Fig. 9, after launching dimensionality reduction with manifold learning, two classes of MNIST images are well separated into distinct groups.

B Discussion about Perception Blinding

Sec. 4.3 introduces perception blinding, as an effective mitigation to defeat our proposed SCA. In this appendix section, we further clarify the usage of perception blinding by discussing the workflow of applying perception blinding in real systems. We then give discussions about its usage and other considerations.

Workflow. Fig. 10 depicts the detailed workflow. As already clarified in Sec. 4.3, to use perception blinding, users only need to pick *one* mask i_{mask} to blind all input data. ❶ A user first picks this *universal* mask i_{mask} and processes it with the to-be-protected media software P to pre-compute $P(i_{mask})$. ❷ Then, before processing any private input $i_{private}$ with P, a user should "$\oplus$" it with i_{mask} locally to get $i_{blinded}$, and then feed $i_{blinded}$ to P. ❸ As introduced in Sec. 4.3, i_{recons} reconstructed by the attacker will mostly retain perception contents of i_{mask}. ❹ In contrast, to get the desired output $P(i_{private})$, a user only needs to "$\ominus$" the pre-computed $P(i_{mask})$ from $P(i_{blinded})$.

Application Scope. By masking media data, perception blinding is designed to effectively mitigate manifold learning-based SCA (see evaluation in Sec. 6.3). We notice some existing side channel attacks toward media software [45, 117] which extensively relies on manual efforts. Perception blinding may *not* be effective to mitigate those works, given those attacks generally conduct data byte-level inference. If data bytes can be *losslessly* recovered, privacy leakage could still occur, though such data byte-level reconstruction generally involves considerable *manual efforts* [45, 117]. In contrast, as will be reported in Appx. D, our well-trained framework takes less than 10 seconds to reconstruct 2,000 media inputs. Also, our proposed perception blinding is not applicable to protect crypto libraries. Unlike media data, the feasibility of defining and extracting "perceptions" over private keys is unclear. Standard blinding techniques (e.g., RSA blinding [21]) should be used to prevent crypto systems from SCA.

"White-Box" Attackers. Readers may wonder what if a "white-box" attacker trains autoencoder with the dataset that includes i_{mask}. We clarify that the mitigation should still be effective, whose reasons are threefold. First, since users *randomly* choose masks, it's impossible for attackers to guess what the mask is. Second, if attackers use a training dataset containing i_{mask} but don't know which one it is, our perception blinding still works. Third, suppose this particular i_{mask} is known, attackers will need to mask all training data and re-train another model, leading to a high cost. Note that "$\ominus$" i_{mask} from i_{recons} will *not* get $i_{private}$, because "$\ominus$" operates on *byte-level* rather than *perception-level*. To understand this, suppose $i_{private}$ is a human face photo toward left, whereas the

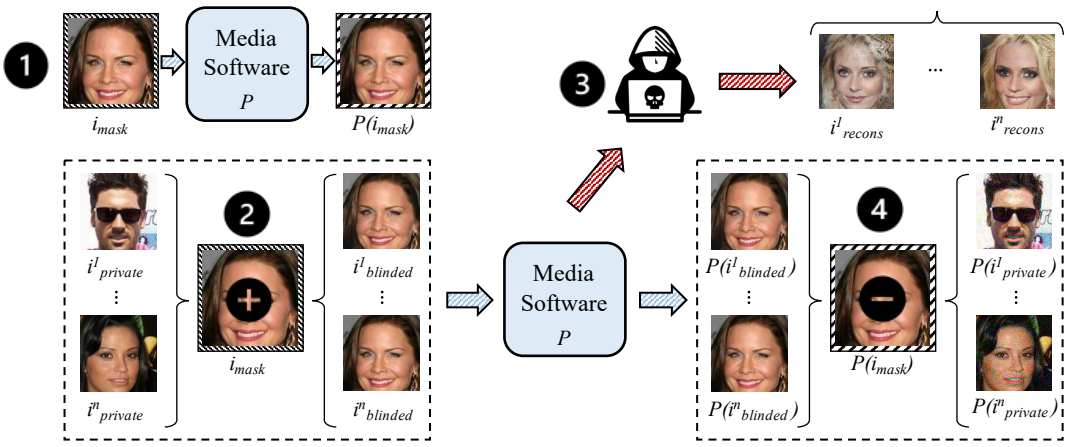


Figure 10: Workflow of perception blinding.

human face in i_{mask} is toward right. As a result, face recovered in i_{recons} should be toward right as well. It's easy to see that "$\ominus$" i_{mask} from i_{recons} will not flip the face direction.

C Attack Setup

We give a general introduction of each side channel adopted in our attack as follows:

Cache Bank. Cache bank generally denotes the minimal storage unit of modern CPU caches and has been exploited by real-world attacks [121]. Assume a program memory address has N bits, then typically the upper $N-L$ bits map a memory access to its corresponding cache bank access. In this research, we adopt a common setting for most CPUs on the market where L is 2. That is, given a memory address $addr$, its cache bank index can be computed as $addr \gg 2$.

Cache Line. Similar to cache bank, attackers can also log all the accessed cache line indexes for exploitation [45, 120]. For modern CPUs whose cache-line size is usually 64, the cache line index of a memory address $addr$ can be computed as $addr \gg 6$.

Page Table. Program virtual memory accesses are converted into corresponding physical memory accesses by querying the OS page table. Given an adversarial-controlled OS, a practical high-resolution side channel is to keep track of all accessed page table entries made by the media software [117]. Given a memory access with address $addr$, the induced page table index can be calculated by masking $addr$ with `PAGE_MASK` m: $addr \,\&\, (\sim m)$, where m set as 4095 [6].

Media Software and Inputs. We use `libjpeg`, a widely-used image processing library, to process two image datasets CelebA and Chest X-ray. CelebA comprises 10,000 different celebrities, with 20 images of each. Chest X-ray comprises real-life X-ray images that are used for screening and diagnosis of many lung diseases. In addition, we use a popular media software, `FFmpeg`, to process two audio datasets, SC09 and Sub-URMP. Both datasets are commonly-used in benchmarking audio synthesis and analysis research [26, 27, 38]. SC09 denotes real-world "speech commands." It contains single spoken words from 0—9 by various speakers in real-life scenarios. Sub-URMP consists of audio recordings of 13 musical instruments, such as double bass, viola, and violin. `Hunspell`, a popular spell checker used by commercial software, such as Google Chrome, OpenOffice, and LibreOffice, is also exploited in this research. We use two datasets, COCO and DailyDialog, as the inputs of `Hunspell`. COCO is a popular large-scale dataset that contains images and text descriptions. Each image is associated with three to eight manually-annotated sentences. Each sentence contains a number of object and attribute names that denote how humans would describe a photograph of a real-world scenario. The DailyDialog dataset contains real-life multi-turn dialogues, which reflect daily communication and cover various topics.

Tools Used in Evaluations. We leverage Face++ [5], a commercial face recognition API, to calculate the similarity score between reconstructed face photos and reference inputs. We clarify that the implementation details of Face++ is *not* disclosed. To decide the diseases of reconstructed X-ray images and reference images, we reuse the tool provided by the champion of CheXpert competition [4]. This tool can categorize the disease of X-ray images and localize corresponding lesions.

When launching quantitative evaluation to measure the privacy leakage of reconstructed audio data, we launch an experiment to train two classifiers for speaker identity and command 0–9 matching. This denotes a typical setup of identity de-anonymization attack [123]. We now report the details of two classifiers. To classify the content of each human voice, we reuse the architecture of our "Privacy-Aware Indicator" in Sec. 4.1. The classifier is trained on reference audio recordings to achieve over 98% testing accuracy. We then use the trained classifier to classify the reconstructed audio. Note that

the identities of training and testing splits are *not* overlapped, and we modify the training objective based on a face recognition model [91]. When evaluating, the accuracy is calculated as how many reconstructed audio recordings yield a similarity score that is higher than 50% with its reference audio (i.e., the correct match).

In addition, when quantitatively evaluating the musical instrument types of reconstructed audio using the Sub-URMP dataset, we also reuse the architecture of "Privacy-Aware Indicator" and train the classifier on reference audio to achieve a testing accuracy higher than 98%. Then, the trained classifier is used to classify the reconstructed audio clips.

D `Prime+Probe` Attack Details

In this section, we clarify the detailed setup of our `Prime+Probe` attack. We consistently assume that attackers can first train the autoencoder framework with cache side channel locally collected via `Prime+Probe` toward victim software, but do *not* need the source code. Then, the attacker launches `Prime+Probe` toward the target media software to log cache side channels when it is processing an unknown input. The unknown input will be reconstructed from the logged cache side channels.

Probing the L1I and L1D Caches. We use Mastik [119] to launch `Prime+Probe` attack towards L1D cache and L1I cache on Intel Xeon and AMD Ryzen CPU. We use Linux `taskset` to pin the `victim` software and a `spy` process to the same CPU core. We take a common assumption [102] that attackers know when the victim media software begins and ends to process an unknown input. The `spy` process primes and probes the cache. Technically, there is another "coordinator" process on the same core which computes victim process's cache activities and logs the cache side channels to disk. Nevertheless, according to our observation, this coordinator process has generally consistent cache access patterns, and therefore, its mostly fixed cache access does not interfere with our well-trained autoencoder.

The thresholds of deciding cache hit and cache miss are 120 CPU cycles on Intel Xeon CPU and 100 CPU cycles on AMD Ryzen CPU. `Prime+Probe` is performed in the following manner:

PRIME: The `spy` process fills all cache sets.

IDLE: The attacker logs the access time of all cache sets for the previous `Prime+Probe` iteration. As a result, the idle phase *interval* equals the duration of performing one file I/O operation. Meanwhile, the cache is utilized by the `victim`.

PROBE: The `spy` process refills all cache sets and times the duration to refill the same cache sets to learn how `victim` accesses cache sets.

For a cache set, the logged cache status flip, from hit to miss, indicates at least one cache access of `victim`. We are thus particularly interested in logging such status flip. We name such cache status flips as "cache activity" in the rest of this paper. Whenever a cache activity is observed, we record the cache activities of the all cache sets into a vector V, whose length equals to the number of cache sets. $V[i] = 1$ indicates there is a cache activity in i-th cache set. In other words, the i-th cache set is accessed at least one time by the `victim`. If no cache activity is observed from any cache set, we omit to generate a new V.

Cache Set Activities Logged by `Prime+Probe`. Fig. 11 presents a recorded sequence of vectors V on L1D cache of Intel Xeon CPU when `FFmpeg` is processing an audio input. Here, each row represents a cache set and each column is a recorded V. The color block indicates there is a cache activity. Consequently, the logged side channel trace of L1 cache is in the format of a binary matrix, where bit 1 represents a cache activity. The binary matrix is taken as the input of our framework in an end-to-end manner. See Appx. F for clarification on representation of side channel traces and how they are fed into the encoding step. Furthermore, the code of launching `Prime+Probe` is released at [3] for result verification and benefiting future research.

Statistics of Logged Cache Side Channels. Table 15 presents the mean, the standard deviation and the matrix encoding of logged side channel traces under different settings. Overall, the standard deviation of trace length is seen as high. This indicates the difficulty of exploiting real-world media software. In general, different inputs can lead to the execution of different code paths, which further induce unaligned cache accesses. To ease the deviation of `Prime+Probe`, we take a simple but effective trick to repeatedly execute media software with the same input for t times and concatenate the logged side channels as one input of our framework. The value of t is set to 8 for `libjpeg` and `Hunspell`, and 4 for `FFmpeg`. In particular, when benchmarking `FFmpeg`, the stddev can grow to half of the average trace length. We view this explains the relatively low attack accuracy of attacking `FFmpeg` using cache side channels recovered by `Prime+Probe`: as shown in Table 12, attack accuracies toward `FFmpeg` are generally below 15% except the Intel CPU & L1D Cache setting.

Workload. We have reported the workload in Table 12, where the incurred execution slowdown is generally within 2 to 10 times compared with the normal execution. Overall, all three media software benchmarked in this study is much complex than crypto libraries like AES. With more cache accesses occurring during execution, cache misses incurred by `Prime+Probe` attack can presumably slowdown the execution of victim software in an effective way. In particular, our attack on `FFmpeg` incurs relatively larger slowdown. This is reasonable: `FFmpeg`, as the most complex software among these three, produce a large volume of cache accesses, which, accordingly increase the slowdown due to numerous cache misses. Nevertheless, we still point out that even for the `FFmpeg` case, the average slowdown incurred by

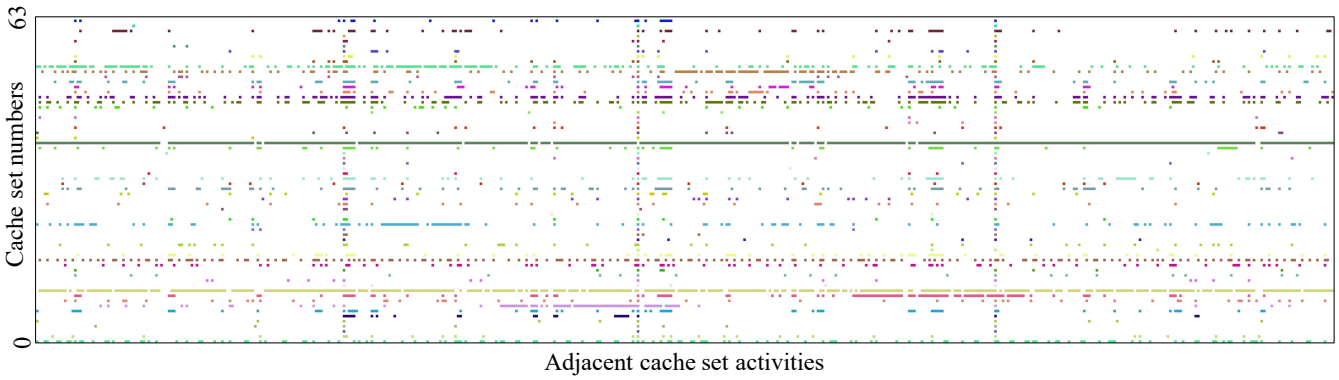


Figure 11: Cache set activities of `FFmpeg` logged by `Prime+Probe` on Intel CPU L1D cache. Colored blocks denote cache access activities, i.e., "hit" flips to "miss". We use different colors to differentiate different cache sets.

Table 15: Statistics (*mean*±*stddev*) and matrix encoding of cache side channel traces logged by `Prime+Probe`. Each trace is a sequence of vector with length 64. Note that the #training and #test splits in each of the evaluation setting are the same as statistics reported in Table 3.

	`libjpeg`(×8)		`FFmpeg`(×4)		`Hunspell`(×8)	
	Intel	**AMD**	**Intel**	**AMD**	**Intel**	**AMD**
L1I Cache	2719 ± 745 $1 \times 256 \times 256$	1114 ± 290 $1 \times 256 \times 256$	44315 ± 23374 $8 \times 512 \times 512$	7013 ± 2540 $2 \times 512 \times 512$	4834 ± 1788 $4 \times 256 \times 256$	1865 ± 432 $2 \times 256 \times 256$
L1D Cache	780 ± 137 $1 \times 256 \times 256$	5750 ± 931 $4 \times 256 \times 256$	8837 ± 3050 $2 \times 512 \times 512$	46698 ± 35163 $8 \times 512 \times 512$	3739 ± 164 $4 \times 256 \times 256$	9732 ± 1498 $8 \times 256 \times 256$

`Prime+Probe` is about 500 milliseconds. We have demonstrated the highly effective `Prime+Probe` attack results toward these media software in Sec. 6.4. To reduce the slowdown and deliver more stealthy attacks, attackers can prolong the idle phase of `Prime+Probe`.

Running Time. In general, running time primarily includes two aspects: 1) online side channel logging and 2) offline model training. To collect side channels for training, we spend 54 hours for `libjpeg`, 36 hours for `FFmpeg`, and 100 hours for `Hunspell` on one CPU core. We note that processing and converting the logged lengthy traces into "Tensor", the legitimate input format of PyTorch, takes several extra hours. After excluding those file processing cost, the logging duration is 9 hours, 12 hours, 27 hours for `libjpeg`, `FFmpeg` and `Hunspell`, respectively. As a research prototype, we use Python for those tedious file processing task. To speed up, users can re-write those codes in C, if needed. The offline model training takes 10 hours.

The "training phases" using cache side channels collected by `Prime+Probe` can likely take *several hours to several days*: for instance, Zhang et al. [124] spend six to 46 hours for the training phase when launching `Prime+Probe` to extract crypto keys. Media software is generally more complex than crypto libraries. We attribute our promising training cost (comparable to [124]) to: 1) recent advances in neural networks and the underlying high-quality deep learning framework PyTorch, and 2) better hardware acceleration since we use one Nvidia GeForce RTX 2080 GPU for training. The "testing phase" of `Prime+Probe`, i.e., reconstructing the unknown input by using a cache side channel trace logged by `Prime+Probe`, takes less than 10 seconds to reconstruct in total 2,000 media inputs.

Qualitative Evaluation Results. We have presented quantitative evaluation results using `Prime+Probe`-recovered cache side channels in Table 12. Most extra (qualitative) evaluation results for attacks based on `Pin`-logged traces are reported in Appx. G. For the seek of readability, we discuss the qualitative results, in terms of reconstructed media data using `Prime+Probe` attack, in this section. Particularly, Fig. 12 and Fig. 13 report reconstructing CelebA face photos on different CPUs. We interpret the reconstruction results as generally promising: a considerable number of visual perceptions are faithfully retained in the reconstructed images, which include gender, face orientation, skin color, nose shape, and hair styles. There is a bit quality degradation on some images, for instance, facial details (e.g., the appearance of teeth) are not always precisely aligned with reference inputs. However, we emphasize that images reconstructed under four settings all manifest comparable visual quality, indicating high feasibility of applying our framework on the basis of commonly-used

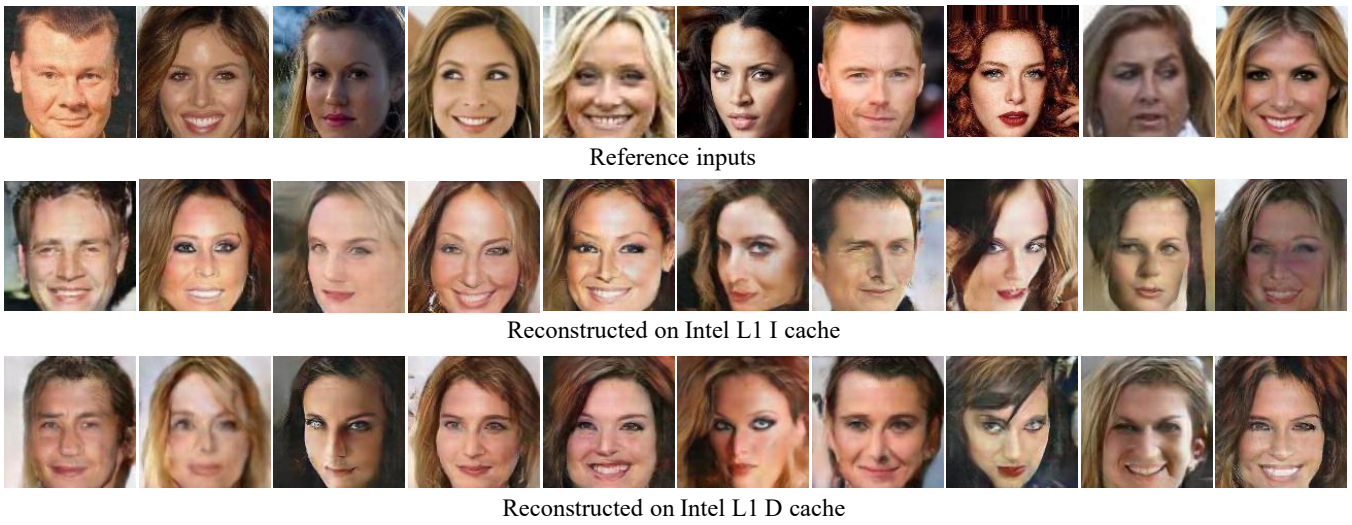


Figure 12: Reconstructed images on L1 cache of Intel Xeon CPU. We can observe highly correlated visual appearances, including gender, face orientation, skin color, nose shape, and hair styles.

Table 16: Musical instrument type matching evaluation results.

	Cache bank	Cache line	Page table
Content accuracy	33.4%	32.8%	32.7%

side channels. The qualitative results are also consistent with results reported in Table 12 — though the attack is launched on different CPUs and different caches, privacy leakage is steadily notable.

E PathOHeap Setup

Sec. 6.5 explored using PathOHeap to mitigate our proposed SCA. PathOHeap, as a popular ORAM protocol, enforces probabilistic memory trace obliviousness, such that it converts input-dependent memory access traces into indistinguishable traces that provably hide input-dependent memory access behavior and information leakage.

We study how ORAM can mitigate our SCA exploitation on `libjpeg`. Our tentative study shows that it takes over one hour to process the entire memory trace using PathOHeap but cannot finish. Hence, we separately extract two key functions from localized vulnerable modules, `IDCT` and `MCU`, that primarily contribute to attacking `libjpeg` (see Table 7). We thus collect much shorter memory access traces corresponding to each function. We then pad all traces to the same length (which is required by ORAM protocols) and use PathOHeap to convert each logged memory access trace into an indistinguishable memory trace, which takes about one minute to process. We then convert the original memory traces and their corresponding ORAM outputs into cache line access traces, and re-launch our SCA exploitation to recover `libjpeg` input images.

F Side Channel Representation & Encoder Design

This section clarifies the representations of input side channels. We also provide empirical results to explain why the representations work well in our research context.

As aforementioned in the evaluation, we launch attacks using side channel traces logged by `Pin`; this can mimic previous attacks where privileged system software, e.g., OS kernels, are controlled by adversaries [45, 117]. We also launch standard `Prime+Probe` attack to benchmark userspace-only scenarios [102, 124]. As shown in Fig. 14, each side channel trace collected by `Pin` contains a sequence of records, and each record denotes one accessed cache unit or page table entry index. Fig. 14 further shows how side channel logs are collected and organized using `Prime+Probe` attack. Here, each trace composes a sequence of binary vectors V, where the cardinality $|V|$ of each vector equals the number of cache sets (the value is 64 in our CPU). $V[i] = 1$ indicates the i-th cache set is accessed by victim.

Encoder Design & Clarification on Its Noise Resiliency

Our autoencoder framework is shown as effective to comprehend even lengthy side channel records logged by either `Pin` or `Prime+Probe`: side channel traces are lengthy albeit highly *sparse*, where only a few elements are *secret-dependent*. Also, the secret-dependent records are not always aligned, given

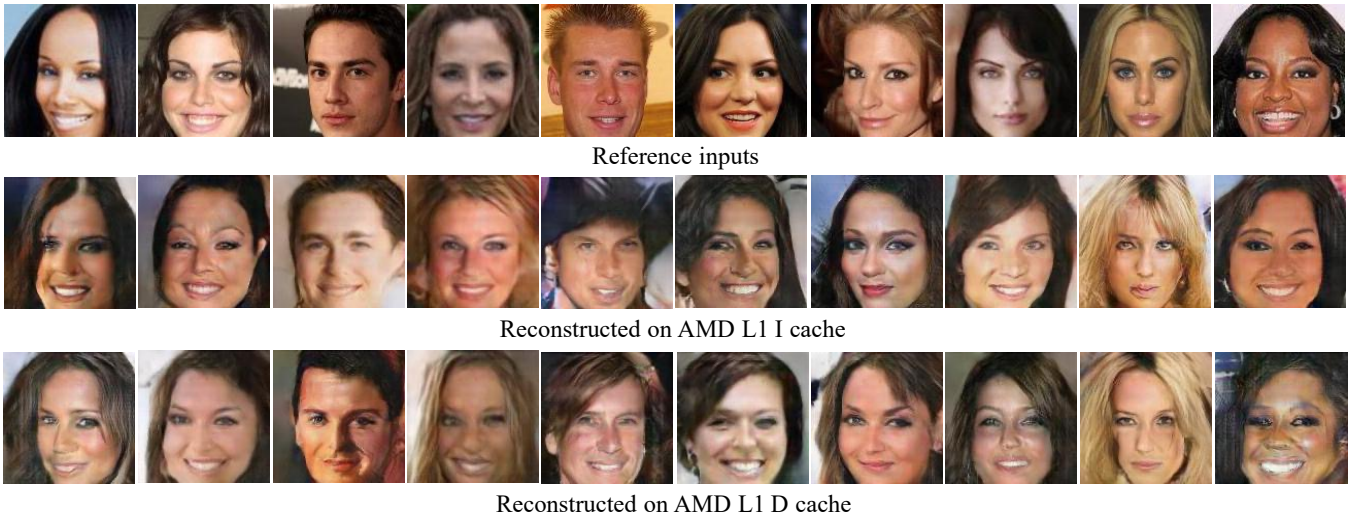


Figure 13: Reconstructed images on L1 cache of AMD Ryzen CPU. Again, visual appearances in the reconstructed images are correlated with reference inputs, including gender, face orientation, skin color, nose shape, and hair styles.

that inputs of different values may lead to executing different paths. Hence, the secret-dependent records may appear at different (relative) locations on a trace in accordance with different inputs. In addition, our noise resilience evaluation in Sec. 6.6 illustrates highly encouraging *robustness* and *resilience* of our autoencoder framework toward perturbations on side channel traces.

In Sec. 4.1, we have clarified that manifold learning itself manifests high capability of denoising. In this section, we further analyze the noise resilience from the encoder model structure perspective. Overall, before feeding a trace (logged by `Pin` or `Prime+Probe`) to our framework, each trace is first folded into a squared matrix with zero-paddings. Fig. 14 depicts how a 2D CNN block of trace encoder ϕ_θ operates on the folded matrix. A Conv2D block has C kernels with each of shape $K \times K$ ($K > 1$) and the input is a matrix of shape $C \times H \times H$. Each kernel has its own parameters and operates on one $H \times H$ section of the input. As the standard operation (see Fig. 14), the kernel moves on the $H \times H$ section step by step, and therefore, all $K \times K$ regions in a section share the same kernel. In general, this classic design ensures an important property named *translation-invariance* [63]. As shown in Fig. 14, suppose the secret-dependent records in the training traces only appear at the blue locations, the ϕ_θ can still capture secret-dependent records at the red locations in a testing trace. Therefore, even noise is introduced, the trace is still sufficiently informative unless all privacy-related records are vanished. In short, the well-known translation-invariance property enforced by our encoder can properly improve the generalization and simultaneously guarantee the robustness towards noise.

Table 17: Disease diagnosis matching rates of reconstructed chest X-ray images w.r.t. (cache bank/cache line/page table) side channels.

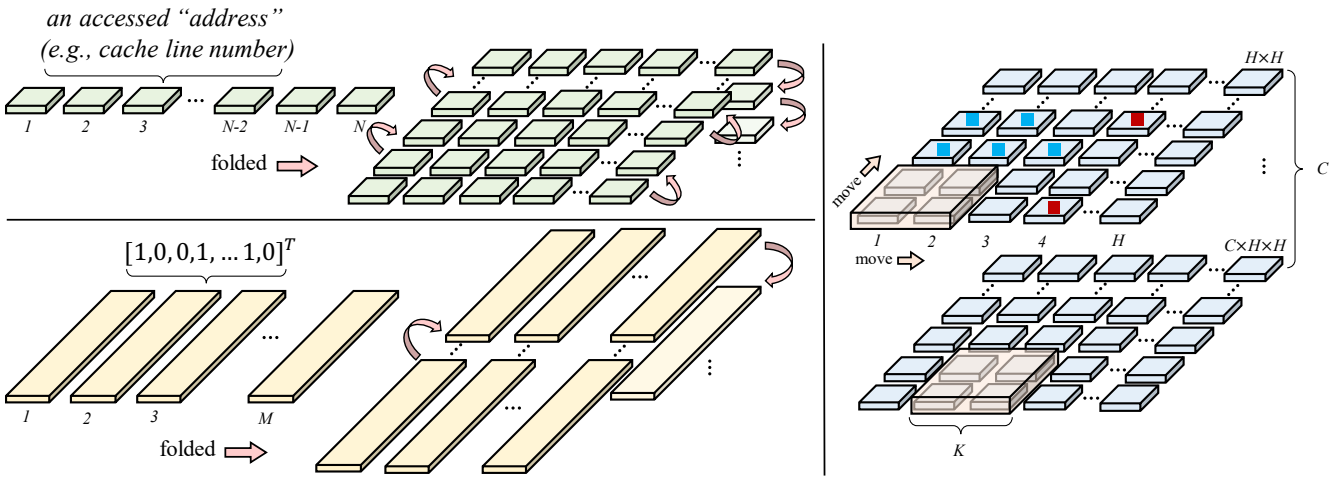
Disease	**Cardiomegaly**	**Consolidation**	**Atelectasis**
Precision	0.74/0.74/0.74	0.75/0.76/0.75	0.83/0.83/0.83
Recall	0.55/0.55/0.54	0.91/0.91/0.91	0.67/0.67/0.67
F1 Score	0.63/0.63/0.62	0.82/0.82/0.82	0.74/0.75/0.74

We are *not* claiming credits from the model design; noise resilience derived from translation-invariance is well studied in the AI community [63, 123]. Nevertheless, we spend efforts to explore other possible model structures at this step, which are seen to manifest lower robustness toward noise. For instance, each record can be attached to a unique weight (e.g., using a fully connected layer or a RNN to process the trace). Consequently, any small perturbation, potentially due to false cache hit or wrong orders, is seen to induce notable change in outputs.

G SCA Results

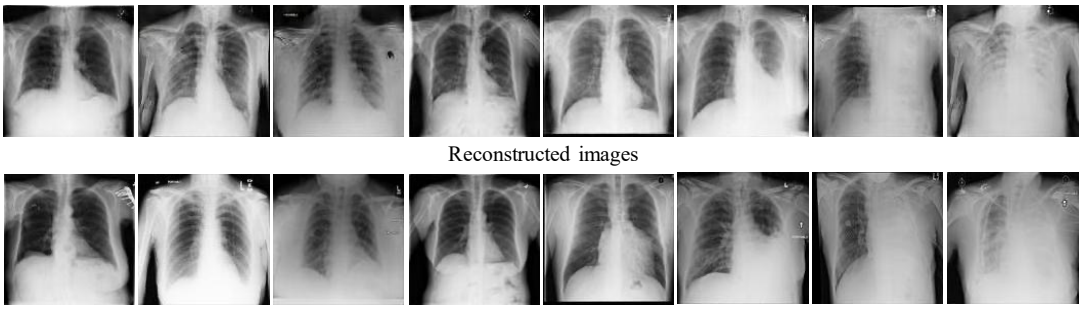
This Appendix presents more reconstructed media data and compares them with the reference inputs in Fig. 15, Fig. 16, Fig. 18, Fig. 19, Fig. 22, and Fig. 23. We also report the quantitative evaluation results of Sub-URMP dataset in Table 16.

Similar to the promising results in reconstructing face images reported in the evaluation section (Sec. 6.3.1), Fig. 15 and Fig. 16 show highly encouraging findings of recovering chest X-ray images from side channel traces. Overall, we note that the recovered X-ray images all manifest high



(a) Fold a trace into a matrix (b) A folded matrix operated by 2D CNN

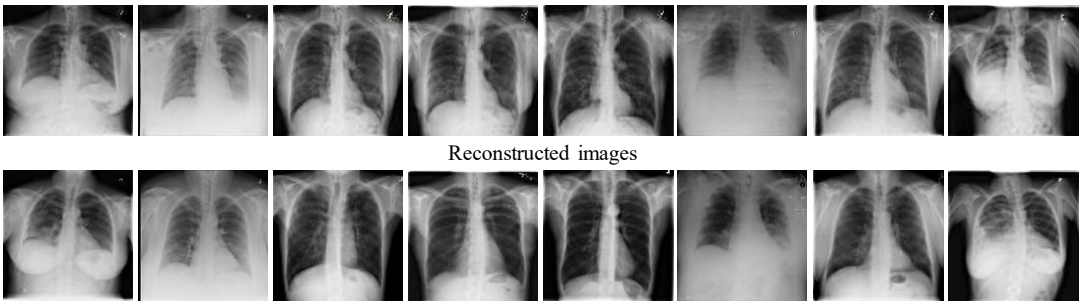
Figure 14: Representation and processing of side channel traces. Traces collected by `Pin` and `Prime+Probe` are marked in green and yellow, respectively. Two types of traces are processed by trace encoder of the same model structure. In general, our encoder enforces an important property named *translation-invariance*. Suppose the secret-dependent records in the training traces only appear at the blue locations, the ϕ_θ can still capture secret-dependent records at the red locations in a testing trace. Therefore, even noise is introduced, the trace should still be reasonably informative unless all privacy-related records are completely vanished.



Reconstructed images

Reference inputs

Figure 15: Qualitative evaluation results of Chest X-ray.



Reconstructed images

Reference inputs

Figure 16: Qualitative evaluation results of Chest X-ray.

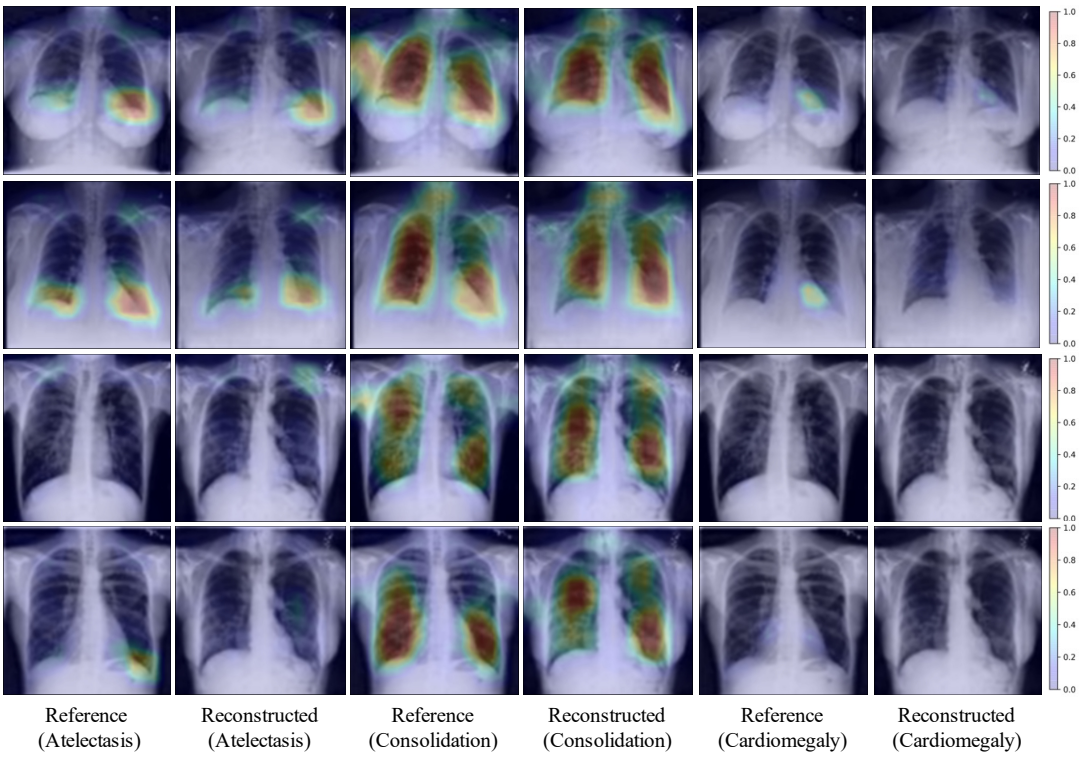


Figure 17: Localized lesions of Chest X-ray.

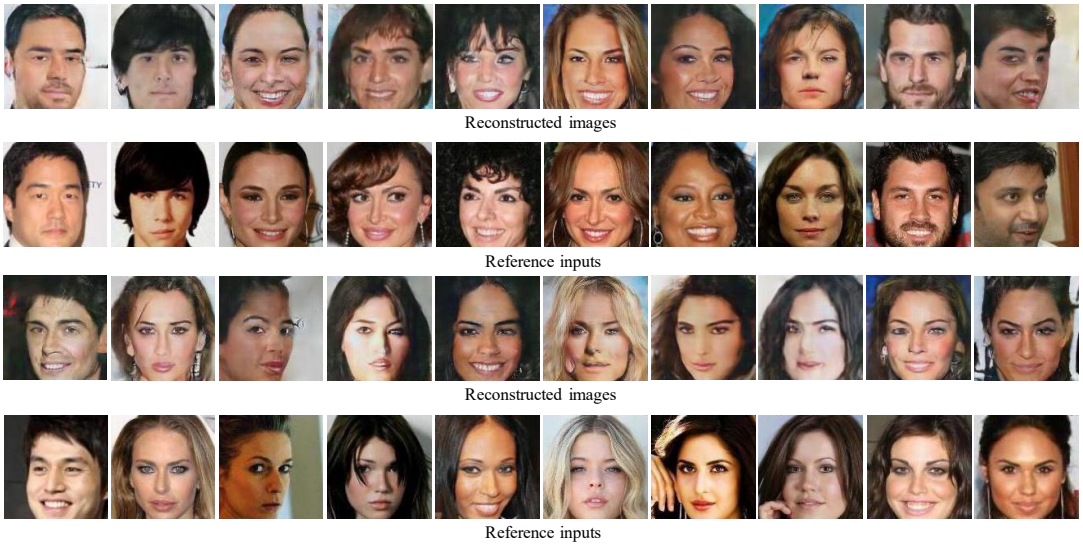


Figure 18: Qualitative evaluation of CelebA.

visual quality and plausible similarity with the reference inputs. Chest X-ray images contain generally less perceptual features compared with CelebA, indicating an easier task for manifold learning-based dimension reduction. On the other hand, we note that X-ray images are of high resolution. To get the best results in disease diagnosis, it is generally required that the recovered X-ray images preserve original details in the reference inputs. Table 17 reports the quantitative evaluation of chest X-ray images. We check whether the same kinds of diseases can be diagnosed from the reference and reconstructed inputs, which would indicate serious privacy leakage. Considering three diseases listed in Table 17, we

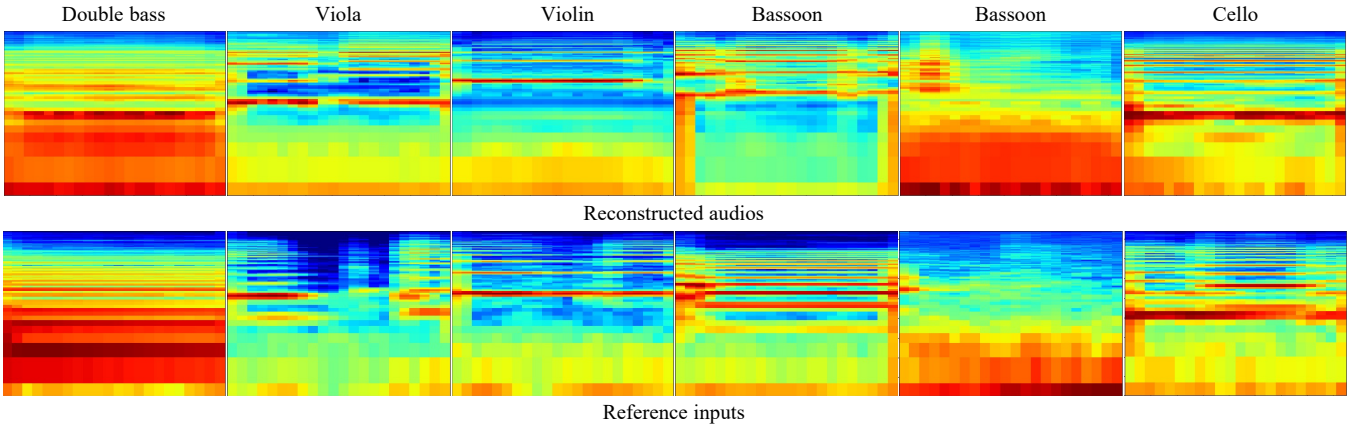


Figure 19: Qualitative evaluation of Sub-URMP. The horizontal axis of each LMS figure represents time from 0s to 0.5s, while the vertical axis represents frequency from 0Hz to 8192Hz.

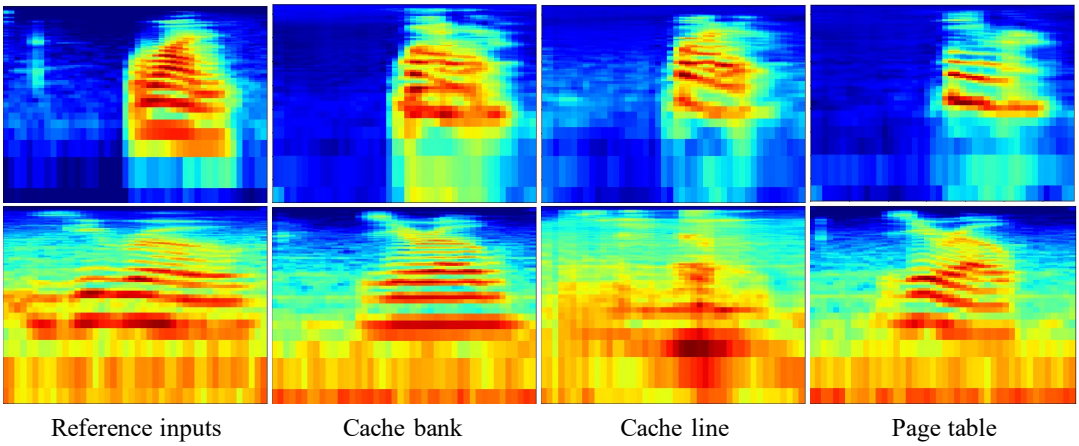


Figure 20: Qualitative evaluation of SC09. The horizontal axis of each LMS figure represents time from 0s to 1s, while the vertical axis represents frequency from 0Hz to 8192Hz. The first row is LMS figure of speaking "one", whereas the second row is speaking "zero."

first train a disease classifier C (see Appx. C) that achieves an F1 score above 98.0% over the reference inputs. Then, let true positive TP be the diagnosis of the same disease d by C from both reference and reconstructed X-ray images. False positive FP of a disease d implies that d is diagnosed from the reconstructed chest X-ray image but not diagnosed from the input. Similarly, false negative FN indicates that a disease is diagnosed from the reference input but it does not from the reconstructed image. We can thus compute the precision ($\frac{TP}{TP+FP}$), recall ($\frac{TP}{TP+FN}$), and F1 score (harmonic mean of the precision and recall), respectively. Overall, Table 17 indicates that accurate disease information can be inferred from the reconstructed X-ray images.

The high accuracy in conducting disease diagnosis over reconstructed images in Table 17 indicates a serious leakage of patient's confidential information. We also localize lesions (see Appx. C clarifying attack setup at this step) of reconstructed X-ray images and corresponding reference inputs in Fig. 17: lesions in reconstructed images and reference inputs are highly consistent.

Fig. 20 reports the evaluation results of reconstructing audio data in LMS graphs, whose x-axis represents time and y-axis denotes log-amplitude of frequencies. The references and reconstructed recordings have mostly consistent LMS graphs in all cases. As mentioned in Table 3 and Appendix C, SC09 includes real-world "speech commands"; hence, recovering quality voice recording indicates a strong likelihood of violating user privacy, such as voice commands. Given that the LMS graphs of audio clips are usually too dense to read on paper, we have also released reconstructed audio

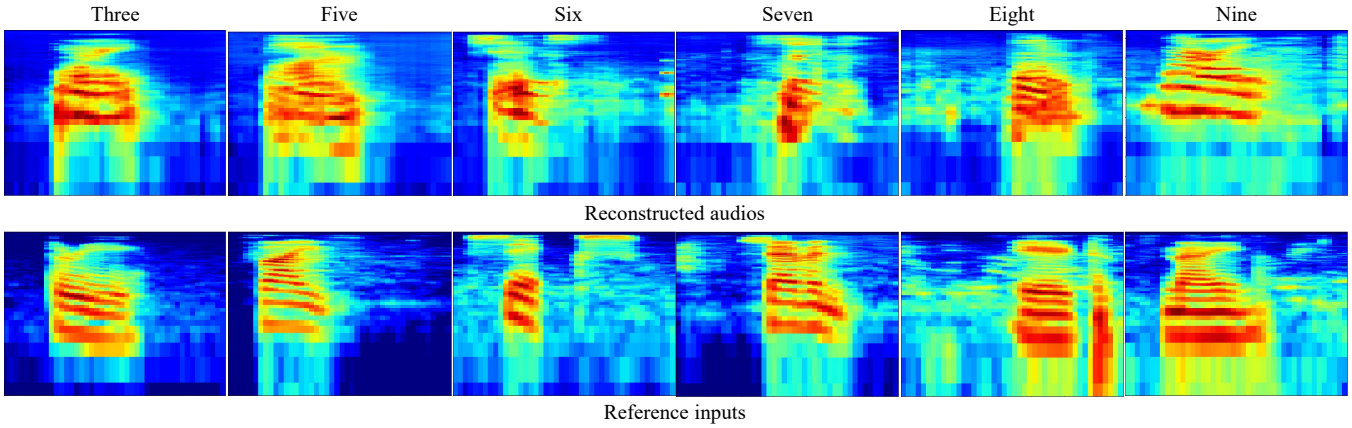


Figure 21: Qualitative evaluation of SC09. The horizontal axis of each LMS figure represents time from 0s to 1s, while the vertical axis represents frequency from 0Hz to 8192Hz.

Reconstructed Text	Reference Input
*<UNK> I supposed to do **now** ?*	*What am I supposed to do then ?*
***I have** , the sunshine and **beautiful up** me **to the** honeymoon . The island , the sound of the <UNK> , the salty **style** air and the sunshine . . .*	*You know , the sunshine and wind remind me of our honeymoon . The island , the sound of the waves , the salty sea air and the sunshine . . .*
Mam , another minute , could I ?	*Mam , another minute , could I ?*
***It ' s** like a good idea .*	*That sounds like a good idea .*
*I <UNK>' t want to insult Jill or her **brother** . I think Jill **,** could be it . But I ' **ll** rather have some **to** little older .*	*I don ' t want to insult Jill or her mother . I think Jill maybe could do it . But I ' d rather have someone a little older .*
*I think it **'** be better **for find** a good babysitter here . It **' be cost , an** or three days .*	*I think it would be better to have a good babysitter here . It might even be for two or three days .*
*She **is** a **single** cold , and **it** don ' t want to take **care to** us . But we don ' t like **how** can stay with our .*	*She has a bad cold , and we don ' t want to take her with us . But we don ' t know who can stay with her .*
*This is **very** <UNK>, I **have** . But Hank and I are leaving tonight .*	*This is short notice , I know . But Hank and I are leaving tonight .*
*I ' m sorry **, say that** . What ' s wrong with her ?*	*I ' m sorry to hear it . What ' s wrong with her ?*
*Have you ever **been** a parking ticket ?*	*Have you ever gotten a parking ticket ?*

Figure 22: Qualitative evaluation of DailyDialog. We mark ***inconsistent reconstructions***.

recordings [3]; interested readers can easily verify that the reconstructed audio clips exhibit high quality with negligible noise.

Neglecting Non-Privacy Factors. Our manual inspection on the reconstructed images also reveal several interesting cases in As presented in Fig. 24, while the reconstructed images of celebrity faces are of good quality and highly similar to the reference inputs, the reconstructed images do not contain glasses. On one hand, we emphasize that the reconstructed images can be matched to the reference inputs with above 99.9% confidence score using the commercial face recognition APIs provided by Face++. This indicates that the "privacy" related features that can uniquely recognize human identities are successfully preserved in the reconstructed photos. More importantly, we interpret this evaluation has shown the effectiveness of our customized objective functions which aim to retain specific privacy indicators. Recall as defined in Table 1, we enforce our autoencoder framework to particularly retain human privacy related contents like gender. As a result, our autoencoder framework narrows the focus to critical features and facilitates commercial APIs extracting key perceptual

Reconstructed Text	Reference Input
child with a toilet and sink bathtub.	Small bathroom with a toilet and a sink
A bus take off into the sky.	A passenger plane taking off into the sky.
A man is sitting a picture of <UNK> in a bathroom mirror.	A woman is taking a picture of herself in a bathroom mirror.
A <UNK> parked is parked on the side of a street.	A motorcycle that is parked on the side of the road.
A computer sitting and a desktop computer on a wooden desk.	A laptop computer and a desktop computer on a white desk.
A man in a white uniform in a base in front of a crowd.	A man in a uniform standing on a motorcycle in front of a crowd.
Four people standing a grassy field with trees in the background.	Four giraffes in a grassy plain with trees in the background.
A man is on a couch talking on a cell phone.	A man sitting on a post talking on a cell phone.
A woman standing a kitchen preparing a meal.	A chef in a kitchen preparing a meal.
This is a picture of a kitchen with a stove stove.	This is a picture of a kitchen with a chrome stove.

Figure 23: Qualitative evaluation results of COCO. We mark consistent reconstructions.

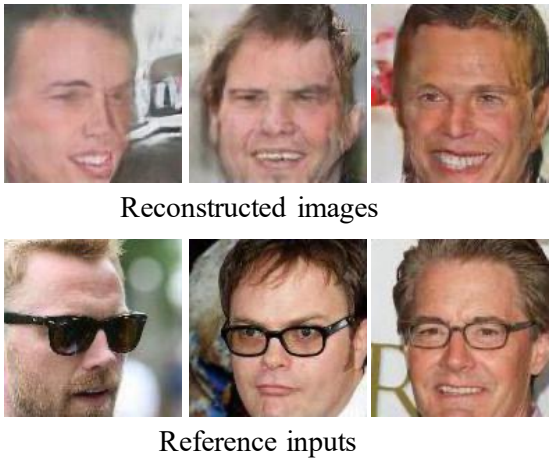


Figure 24: Reconstructed images with no glass attached.

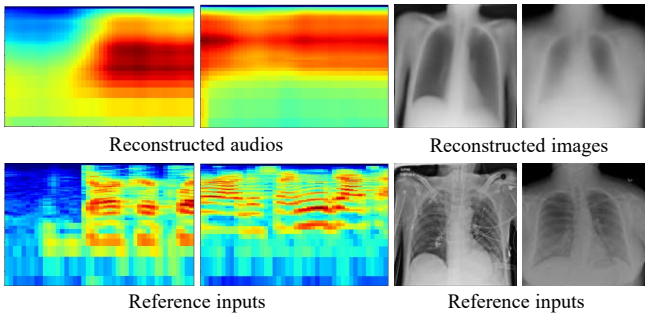


Figure 25: Reconstructed images suffering from over-smoothing.

contents. Non-privacy factors (e.g., glasses) are generally discouraged to distract the attention of our attack framework.

Ablation Evaluations. Recall in designing objective functions, we explain that using only pairwise distance metrics can likely generate "over-smoothing" images, thus clarifying the necessity of composing the objective function with discriminator to implicitly capture the "semantics similarity" among reference and reconstructed images. Fig. 25 presents several reconstructed images by only using the pairwise distance. It is easy to see that the reconstructed images exhibit low quality compared with sample cases shown in Fig. 15 and Fig. 20. In particular, it suffers from over-smoothing, where the *details* in the LMS images and chest X-ray photos become much blur, comparing with the reference inputs. We view the results empirically demonstrate the necessity and strength of adopting hybrid objective functions as the learning goal of our autoencoder framework. Also, mode collapse may be potentially introduced by the implicit objective function. Nevertheless, we clarify that high discriminability of the reconstructed media data empirically demonstrates that mode collapse is *not* a major concern of our framework.

Vulnerable Code. In addition to vulnerable code localized in `FFmpeg` and reported in Sec. 6.2, we further report vulnerable code in `libjpeg` and `Hunspell` in Fig. 26 and Fig. 27, respectively. Both code fragments contain obvious input-dependent memory accesses (we mark program variables derived from inputs in red). These input-dependent memory accesses further lead to the accesses of different cache units or page table entries, thus enabling side channel exploitations. To the best of our knowledge, `MCU` and `putdic`, as vulnerable code fragments of `libjpeg` and `Hunspell`, were not pointed out by existing works [45, 117]. In addition, we identify these

```
1  int HUFF_EXTEND(int x, int s) {
2    // ''ex_test'' and ''ex_offset'' are
3    // pre-calculated arrays
4    if (x < ex_test[s])
5      return x + ex_offset[s];
6    else
7      return x;
8    }
9
10 boolean decode_mcu_fast(j_decompress_ptr cinfo,
11   JBLOCKROW *MCU_data) {
12   huff_entropy_ptr entropy =
13    (huff_entropy_ptr)cinfo->entropy;
14   /* preprocessing */
15   for (int i = 0; i < cinfo->blocks_in_MCU; i++)
16     d_derived_tbl *dctbl = entropy->dc_cur_tbls[i];
17     int s, k, r, l;
18     /* get index ''idx'' based on ''s'' */
19     /* update ''r'' */
20     s = dctbl->lookup[idx];
21     // ''lookup'' is pre-calculated array
22     if (s)
23       s = HUFF_EXTEND(r, s);
24     }
25     /* do something */
26   }
27   /* do something and return */
28 }
```

Figure 26: Vulnerable code components in `libjpeg`. We mark variables depending on `libjpeg`'s input in red, and **bold** input-dependent memory accesses (e.g., line 4).

Table 18: Generalization evaluation.

(k,N)	$(1,100)$	$(5,100)$	$(20,100)$
`libjpeg`	5.7%	20.3%	44.1%
Baseline	1%	5%	20%

stealthy code fragments fully automatically using neural attention mechanisms. This highlights the strength of our neural approach. And to confirm our findings, we manually analyzed how inputs are propagated into certain program variables, and how those program variables are used to access memory (and further lead to side channels).

Also, we report all the localized assembly instructions that primarily contribute to the reconstruction of private inputs. The corresponding line number of localized assembly instructions are reported in [3]. We use the default configuration to compile each media software, whose compiled executable file can also be found in our released repository [3]. Hence, developers can use our reported information and released executable files to further localize and patch relevant code fragments.

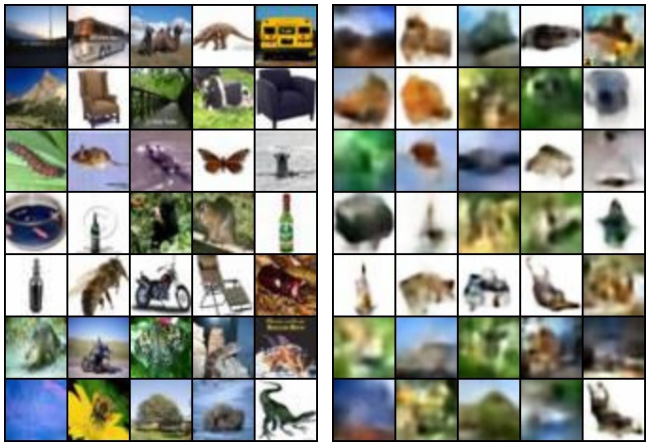
Generalization. As explained in Sec. 3, different types of media data (e.g., human face vs. vehicle photos) are generally projected toward distinct manifold spaces [14, 88, 99]. Hence, training a unified model to recover media data of different classes are beyond the scope of our SCA.

To thoroughly explore the potential limitations, this section provides an empirical assessment of the generalization of our SCA framework. To this end, we collect side channel traces logged when using `libjpeg` to process a general dataset, CIFAR-100 [59]. These side channel traces are used to train our autoencoder framework and to reconstruct unknown images in CIFAR-100 from their induced side channel traces. The CIFAR-100 dataset comprises 60K images of 100 classes. Each class of 600 images is divided into 500 training images and 100 testing images.

Fig. 28 reports the qualitative evaluation results, by comparing the inference inputs with their reconstructed images. In general, we observed that the reconstructed images manifest

```
1  boolean check(Hunspell** pMS, int* d, string& token) {
2    // checking and transforming encoding of ''token''
3    if pMs[*d]->spell(token)
4      return true;
5    return false;
6    // ''pMs'' is a hash table storing the dictionary
7    // spell() performs spell checking
8  }
9
10 int putdic(const std::string& word, Hunspell* pMS) {
11   // checking and transforming encoding of ''word''
12   size_t w = word.find('/', 1);
13   if (w == std::string::npos) {
14     if (word[0] == '*')
15       ret = pMS->remove(word.substr(1));
16     else
17       ret = pMS->add(word);
18   } else {
19     std::string affix = word.substr(w + 1);
20     word.resize(w);
21     if (!affix.empty() && affix[0] == '/')
22         affix.erase(0, 1);
23     ret = pMS->add_with_affix(word, affix);
24   }
25   // ''pMs'' is a hash table storing the dictionary
26   return ret;
27 }
```

Figure 27: Vulnerable code components in `Hunspell`. We mark variables depending on `Hunspell`'s input in red, and **bold** input-dependent memory accesses (e.g., line 3).



Reference inputs | Reconstructed images

Figure 28: Reconstructed images on CIFAR-100.

much worse visual quality than those synthesized from specific datasets (e.g., CelebA and Chest X-ray). Nevertheless, we still observed that some expressive features, particularly sketch and color, are retained in the reconstructed images.

For quantitative evaluation, we use SSIM [110] to assess similarity between reconstructed images and reference inputs. Table 18 reports the evaluation results of determining whether the reference input appears in the top-k of N (e.g., top-5 out of randomly selected 100) images matched with the reconstructed images. The overall matching rates are high and greatly outperform the baseline — random guess. These findings indicate the promising potential of our approach to exploit arbitrary datasets and recover confidential user inputs. Though the reconstructed media data was not visually vivid, it still notably facilities privacy stealth.

Note that a conventional approach in AI community is to provide the class label of each image [18]. In short, the model can switch to proper manifold according to image labels. Our experiment does not provide class labels and mix all images together to faithfully explore model's generalization capability. We leave it as one future work to enhance generalization with labeled data and more advanced models.

H Mitigation

In accordance with Sec. 6.3, Fig. 29 further reports qualitative evaluation results of perception blinding-based mitigation. In short, Fig. 29 manifests results and findings mostly comparable with evaluations launched in Sec. 6.3. That is, "noise mask" (the first row) and "non-face mask" (the second row) are generally not effective in blinding $i_{private}$; perceptual features can be seen in the reconstructed images (e.g., face poses, hair style). Using real face images from the CelebA dataset as the masks manifest highly encouraging results to blind key perceptual-level features. In addition, to recover final outputs (i.e., the "Recovered" columns), a larger α, at least greater than 0.10, should be desirable.

Regarding quantitative evaluation, Table 19 reports the adversary disease diagnosis results after applying three blinding masks toward the Chest X-ray dataset. Consistent with our findings from the CelebA dataset, using "X-ray#1" image to blind chest X-ray images can achieve a much better result to reduce the disease diagnosis accuracy. We also report the quantitative evaluation results of mitigating DailyDialog datasets in Table 21, which manifest mostly consistent results with Table 11.

I Noise Resiliency Evaluation Setup

This section elaborates on the setup of noise resiliency evaluation launched in Sec. 6.6. In sum, we evaluate adding noise to cache line access traces logged by `Pin` and cache set access traces logged via `Prime+Probe` on Intel L1D cache. First, given a `Pin` logged side channel trace, we leverage the following schemes to insert noise into the trace.

Gaussian noise. We perturb every record d on a side channel trace using $d = x \times n + (1-x) \times d$, where $x \in \{0.2, 0.5\}$. n is randomly generated noise following Gaussian distribution.

Removal. We randomly remove $x\%$ of the data points on the side channel, where $x \in \{20, 50\}$.

Round shifting. We round shift a side channel trace for x steps, where $x \in \{10, 100\}$.

Note that each noise insertion scheme has two configurations. For the ease of presentation, we use **Low** and **High** to denote two configurations, respectively. For instance, **Gaussian/High** denotes an intensive setting such that we apply Gaussian noise to perturb side channel traces when $x = 0.5$. As for the cache set access traces logged via `Prime+Probe`, we also launch the following three perturbation schemes:

Leave cache hit/miss out. We randomly drop $x\%$ of the cache set hit/miss records on the logged trace, where $x \in \{20, 50\}$.

False cache hit/miss. We randomly flip $x\%$ of records in the logged cache set access trace, where $x \in \{20, 50\}$. This way, we create false cache hits/misses.

Wrong order of cache hit/miss. We randomly select x non-repetitive cache set hit/miss records and compose $x/2$ pairs of records, where $x \in \{100, 500\}$. We then exchange records in each pair.

Again, each noise insertion scheme has two configurations, and we use **Low** and **High** to denote the intensity of two configurations. In addition, we also mimic real-world noise, by introducing extra workload over the CPU core when launching `Prime+Probe`. Particularly, in our exploitation launched Sec. 6.4, only victim, `spy`, and coordinator processes occupy the CPU core. At this step, however, we launch extra processes on the same CPU core, which can likely introduce a considerable amount of noise on the trace. Particularly, we consider the following three scenarios to systematically explore noise introduced by real-world workload.

Bzip2. We pick the **bzip2** software from SPEC CPU 2006 testsuite to compress a large file (100MB) simultaneously when the `spy` is launching `Prime+Probe` attack toward victim. SPEC CPU 2006 is a standard CPU-intensive benchmark suite that is frequently used in security research.

Victim$_1$. We launch another victim software (e.g., another `libjpeg`) on the same core. This victim software will process the same input simultaneously when the `spy` is launching `Prime+Probe` attack toward victim.

Victim$_2$. We launch another victim software (e.g., another `libjpeg`) on the same core. This victim software will process different inputs simultaneously when the `spy` is launching `Prime+Probe` attack toward victim.

To certain extent, noise introduced by these three workloads could have been subsumed by our inserted noise (e.g., Gaussian or false cache hits/misses). Nevertheless, we still launch this evaluation to thoroughly benchmark the noise resiliency of our SCA.

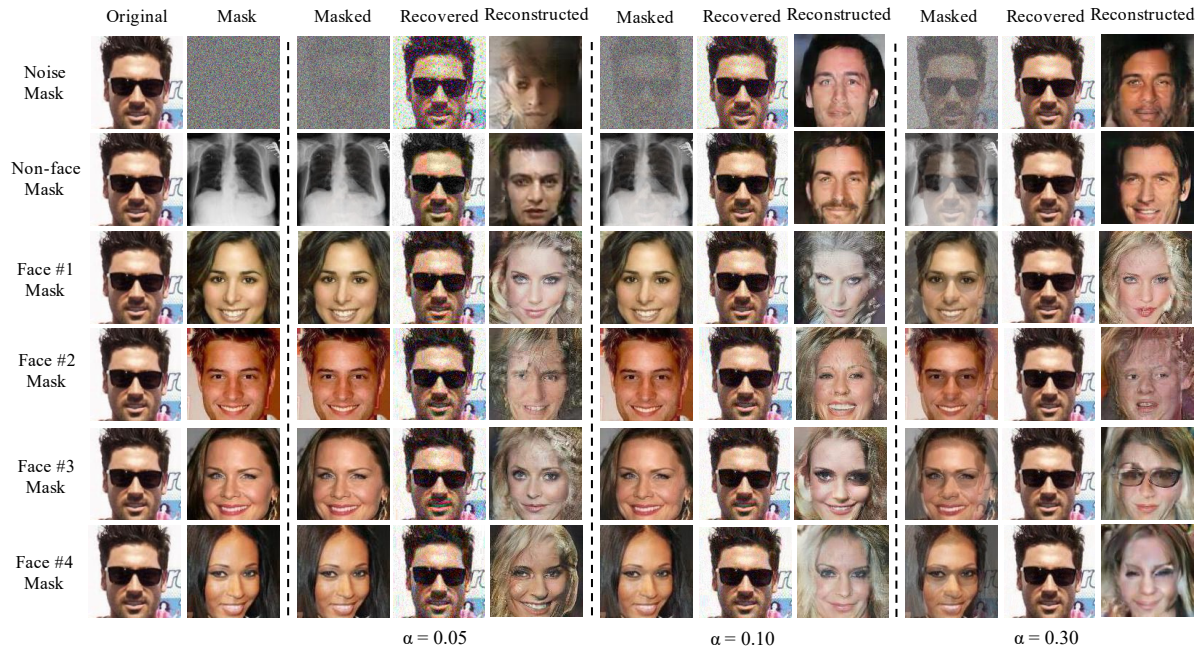


Figure 29: Qualitative evaluation results of perception blinding.

Table 19: Mitigating adversary disease diagnosis attack on Chest X-ray dataset. We report text data inference accuracy in terms of cache bank/cache line/page table. We use three blinding masks as "Noise" "Non-X-Ray" and a real X-ray photo "X-Ray #1".

Mask	Disease	$\alpha = 0.05$	$\alpha = 0.1$	$\alpha = 0.3$
Noise	Cardiomegaly	0.61/0.55/0.54	0.61/0.54/0.53	0.63/0.58/0.53
	Consolidation	0.82/0.82/0.81	0.82/0.81/0.81	0.82/0.81/0.81
	Atelectasis	0.60/0.60/0.57	0.60/0.56/0.57	0.61/0.57/0.55
Non-X-Ray	Cardiomegaly	0.61/0.54/0.58	0.63/0.55/0.56	0.63/0.52/0.51
	Consolidation	0.81/0.81/0.82	0.82/0.82/0.82	0.81/0.81/0.81
	Atelectasis	0.61/0.55/0.58	0.65/0.55/0.58	0.61/0.57/0.54
X-Ray #1	Cardiomegaly	0.15/0.19/0.14	0.20/0.21/0.19	0.20/0.27/0.20
	Consolidation	0.73/0.83/0.79	0.74/0.82/0.80	0.74/0.85/0.83
	Atelectasis	0.08/0.07/0.08	0.12/0.11/0.15	0.19/0.12/0.14

Table 20: Mitigating human voice matching attack on SC09 dataset with blinding. We report text data inference accuracy in terms of cache bank/cache line/page table. We use three blinding masks as "Noise" "Non-Voice" and a real data sample "Voice".

Mask	$\alpha = 0.05$	$\alpha = 0.1$	$\alpha = 0.3$
Noise	13.1/12.8/12.9%	15.2/15.3/15.1%	20.3/19.9/20.1%
Non-voice	14.2/13.9/14.1%	17.1/17.0/17.3%	20.2/20.0/19.8%
Voice	7.2/7.0/7.0%	7.1/7.8/7.6%	8.7/8.5/9.1%

Table 21: Mitigating DailyDialog text inference attack. We report text data inference accuracy in terms of cache bank/-cache line/page table. $\alpha = 0.05$ denotes word appended with total 19 masks. $\alpha = 0.1$ denotes word appended with total 9 masks, while $\alpha = 0.3$ denotes word appended with total 2 masks.

Mask	$\alpha = 0.05$	$\alpha = 0.1$	$\alpha = 0.3$
"I"	0.19/0.32/0.18%	0.18/0.34/0.19%	0.50/0.88/0.38%
"you"	0.22/0.33/0.22%	0.24/0.34/0.26%	0.45/0.72/0.53%

We have reported key results in Sec. 6.6 on exploiting `libjpeg` and reconstructing CelebA face photos. Fig. 31 reports the corresponding qualitative evaluation results. The first column is the reference input and the second column has images reconstructed from `Pin`-logged side channel traces and `Prime+Probe`-logged cache side channels with no noise inserted. Each row represents several configurations with the same intensity. Despite the challenging noise insertion schemes, visually consistent contents (e.g., gender, face orientation, eyes, mouth) between the reconstructed images and reference inputs can still be observed. When perturbing `Pin`-logged traces, reconstructed images under the **Round shift-**

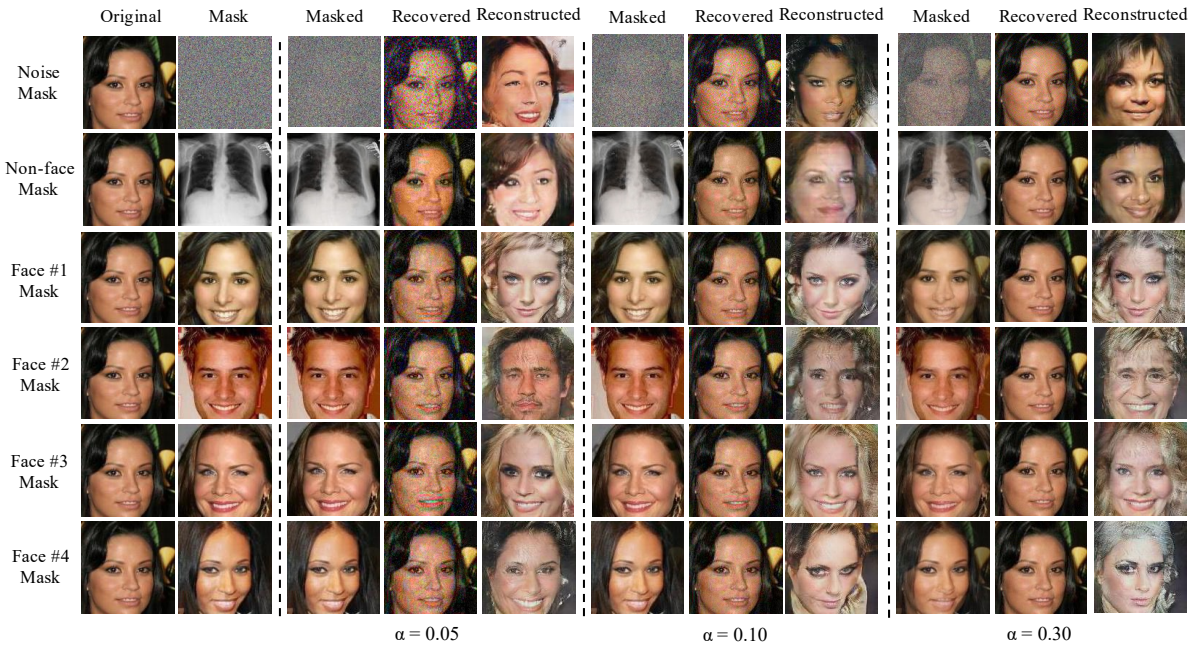


Figure 30: Qualitative evaluation results of perception blinding.

Table 22: Quantitative evaluation results of human voice reconstructed from noisy side channels.

Noise	NA	Low	High
Gaussian	28.8%	20.4%	17.0%
Shift	28.8%	28.6%	26.3%
Removal	28.8%	25.0%	24.5%
Leave hit/miss out	81.8%	80.7%	80.0%
False hit/miss	81.8%	78.5%	3.4%
Wrong order	81.8%	82.1%	79.9%
Bzip2	81.8%	66.0%	
Victim$_1$	81.8%	67.5%	
Victim$_2$	81.8%	55.8%	

Table 23: Quantitative evaluation results of dialog text reconstructed from noisy side channels.

Noise	NA	Low	High
Gaussian	37.4%	35.5%	30.8%
Shift	37.4%	25.6%	27.0%
Removal	37.4%	32.8%	32.6%
Leave hit/miss out	32.2%	32.1%	32.1%
False hit/miss	32.2%	32.2%	32.2%
Wrong order	32.2%	32.0%	32.2%
Bzip2	32.2%	26.4%	
Victim$_1$	32.2%	26.2%	
Victim$_2$	32.2%	25.9%	

ing scheme retain better visual appearances, indicating better noise resilience capability. The **Removal** scheme, which extensively removes records in a trace, triggers obvious quality degradation — some perceptual contents become unaligned. Similarly, **Gaussian noise**, particularly when $x = 0.5$, changes the visual appearances. Nevertheless, as we clarified in the paper, visual appearances change do not necessarily indicate attack accuracy degradation: as reported in Table 14, we still achieve a reasonably high attack success rates even in front of Guarantee noise insertion. After introducing noise into cache side channels collected by `Prime+Probe` (with three schemes presented in the third and fourth rows of Fig. 31), features (e.g., hair style) in reconstructed face images are still primarily aligned with images reconstructed without manual noise. Moreover, increasing noise intensity only leads to negligible changes of facial features. We interpret that these evaluations demonstrate the high resilience of our autoencoder framework toward noisy settings. See our discussion below in **Noise Resilience Analysis**. In addition, it is shown that stressing `Prime+Probe` with extra workload can induce noticeable effect on the reconstructed images. Nevertheless, many perceptual features are still retained in the reconstructed images. Again, we view the results are generally consistent with our quantitative evaluation results in Table 14. See **Noise Resilience Analysis** below for further discussion.

Table 22 and Table 23 further present evaluation results on exploiting `FFmpeg` and `Hunspell`. Round shifting is more effective in mitigating SCA toward text data. We note that round shifting (especially with the **High** scheme) can presumably change the "preceding words" of a to-be-predicted word and is thus more effective in disturbing our decoder of discrete data (see Fig. 2). In contrast, the reconstructed

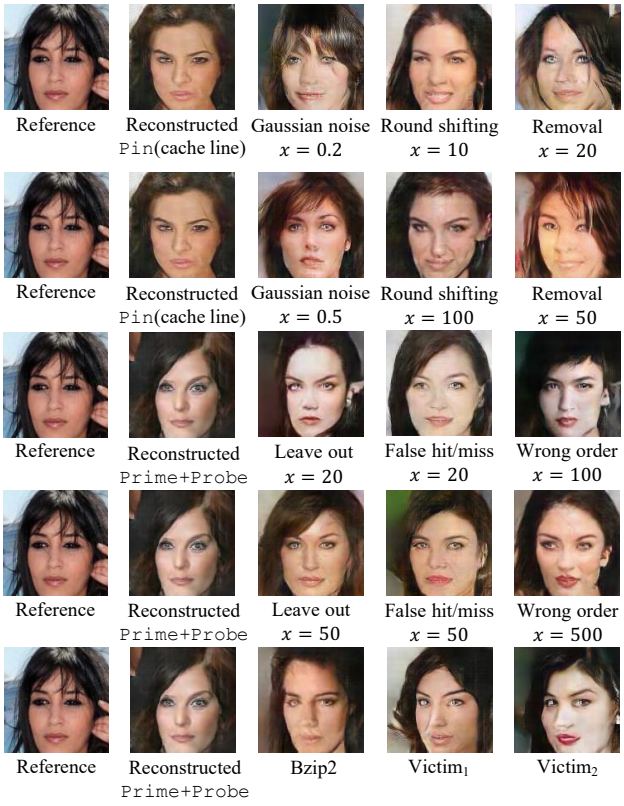


Figure 31: Evaluation results of CelebA dataset in terms of 9 different noise settings.

image and audio data are more resilient toward round shifting. Similar to the libjpeg evaluation reported in Table 14, attack on FFmpeg is notably undermined in front of the **Removal** and **Gaussian noise** schemes. As clarified in Sec. 6.6, these two schemes extensively leave out or perturb data points on the logged trace (e.g., **Removal/High** removes 50% of the records on a trace), show greater influence on data reconstruction. Nevertheless, reasonably high attack accuracy can still be achieved in the presence of perturbed side channel traces. Manifold learning shows encouraging resilience toward noisy inputs. In addition, as clarified in Appx. F, the logged side channel traces are lengthy and highly *sparse*, where only a few elements are informative and secret-dependent. Therefore, the inserted noise does not necessarily break informative data points. We also report promising results that noise on trace collected by Prime+Probe (i.e., the middle three rows) imposes small influence in undermining our exploitation, except the scheme **False hit/miss & High** on FFmpeg. The similar encouraging observations can be found from noise introduced by three real-world workload schemes as well.

Noise Resilience Analysis In line with our discussion on noise resilience offered by manifold learning concept (Sec. 4.1) and neural trace encoder (Appx. F), Sec. 6.6 and this appendix section empirically demonstrate the noise resilience of our attack. We now discuss the noise resilience from the empirical perspective. First, trace collected by Prime+Probe is very noisy with high stddev; when training with such noisy traces, the autoencoder framework is "enforced" to obtain higher generalization, but may sacrifice some accuracy. That is, the robustness and noise resilience is indeed improved when training with side channel records logged via Prime+Probe. Second, as discussed in Appx. F, the logged side channel trace is generally sparse. Suppose only "1", denoting a cache hit $\rightarrow$ miss flip, in a logged trace (collected by Prime+Probe) contributes to reconstructing media data, "Leave out" only drops a small portion of 1. For "Wrong order", since CNN is translation-invariant (as we have introduced in Appx. F), suppose all parameters in a kernel are 1, and two exchanged records are in a $K \times K$ region, then the output will not change, because "convolution" is element-wise multiplication followed by a sum function. Third, the results of FFmpeg increase a lot on Prime+Probe but libjpeg and Hunspell decrease; this indicates that traces collected using Prime+Probe toward FFmpeg is more informative. Therefore, flipping 50% of the records (the **High** scheme) will more likely violate patterns learned by our autoencoder framework despite the translation-invariance. This explains the accuracy drop for noise insertion scheme **False hit/miss & High**. Again, suppose all parameters in a kernel are 1, since in most of the cases, the number of 0 is way larger than 1, flipping records will induce a noticeable impact on the output of convolution operations.